This is a non-peer-reviewed preprint submitted to EarthArXiv.

This manuscript has been submitted for publication in [GEOPHYSICS]. Please note the manuscript has yet to be formally accepted for publication. Subsequent versions of this manuscript may have slightly different content. If accepted, the final version of this manuscript will be available via the 'Peer-reviewed Publication DOI' link on the right-hand side of this webpage. Please feel free to contact any of the authors; we welcome feedback.

Surface Wave Dispersion Calculation and

Sensitivity Analysis in Anisotropic and Weakly

Attenuating Medium Based on Spectral Element

Method

Nanqiao Du*, Tianshi Liu[‡], Mijian Xu[†], Tingwei Yang[§] and Qinya Liu^{*†}

*Department of Earth Sciences, University of Toronto, Toronto, Canada, M5S 3B1

[†]Department of Physics, University of Toronto, Toronto, Ontario, M5S 1A7

[‡]Seismological Laboratory, California Institute of Technology, CA 91125, USA

§ Key Laboratory of Marine Mineral Resources, Guangzhou Marine Geological

Survey, China Geological Survey, Guangzhou 511458, China.

(October 15, 2025)

GEO-Example

Running head: *Geophysics*

ABSTRACT

We present a comprehensive and flexible framework for modeling 1-D surface wave

dispersion in anisotropic and weakly attenuating media. The spectral element method

is employed to accommodate various stress-strain relationships, boundary conditions,

and multiphysics coupling effects. Both radial and general complex anisotropic re-

lations can be incorporated. Standard linear solid models, along with a correction

1

method, are utilized to efficiently model attenuation effects. In addition, we provide a sensitivity analysis framework for any quantity with respect to model parameters using the adjoint method. Three numerical experiments are presented to demonstrate the capabilities and flexibility of our approach. Overall, this study offers researchers a powerful and versatile tool for investigating Earth's subsurface structures.

INTRODUCTION

The variation of elastic parameters in both the shallow and deep Earth plays a crucial role in understanding the dynamics of the Earth's system. Among the most powerful tools for probing the subsurface are surface waves, which can be recorded from earthquake events (Prindle and Tanimoto, 2006; Lin et al., 2009) or retrieved from ambient noise data (Shapiro et al., 2005; Wang et al., 2018; Yang et al., 2024b; Shen et al., 2024). A defining characteristic of surface waves is their dispersive behavior (Aki and Richards, 2002), which becomes particularly significant at different spatial scales. This dispersion underpins a wide range of geophysical applications, from local-scale seismic exploration (Xia et al., 1999; Kugler et al., 2007) to regional studies (Ritzwoller and Levshin, 1998; Shen et al., 2016), and global surface wave tomography (Woodhouse and Dziewonski, 1984; Nishida et al., 2009).

The propagation of surface waves in realistic Earth models is influenced by lateral heterogeneities. Fortunately, under the assumption of slow variation — commonly referred to as the surface wave WKBJ theory (Woodhouse, 1974; Tromp, 1994) — the surface wavefield can be approximated as a superposition of dispersion effects derived from a series of local 1-D models. This approximation necessitates fast and robust computation of surface wave dispersion for a given 1-D model, a fundamental task in surface wave studies. The most widely used approach for modeling surface wave dispersion in 1-D radially anisotropic media is the propagation matrix method (Thomson, 1950; Dunkin, 1965), which has been extended to more general anisotropic media (Park, 1996; Martin and Thomson, 1997). These methods solve the plane-wave,

source-free wave equations within each homogeneous layer and enforce continuity of displacement and traction at layer interfaces to propagate the solution throughout the structure. To improve numerical stability, techniques such as generalized reflection/transmission coefficients have been developed (Luco and Apsel, 1983; Chen, 1993). The final phase velocity is obtained by root-finding algorithms that ensure satisfaction of both the free-surface and radiation boundary conditions (Knopoff and Randall, 1970). For models with complex depth-dependent variations, alternative numerical approaches have been introduced, including numerical integration methods (Takeuchi and Saito, 1972), the finite element method (Haney and Tsai, 2017), and the spectral element method (Hawkins, 2018), all of which have seen broad applications in modern surface wave research.

Attenuation is another critical factor that affects both the amplitude and phase of seismic waves (Carcione, 1995). It arises from various physical processes, including partial melting (Sherburn et al., 2006; Lanza et al., 2020), crustal deformation (He et al., 2021), and fluid effects in rock samples (Yang et al., 2024a, 2025). The effects of attenuation on surface waves have been extensively studied, particularly in the context of body waves and earthquake-generated surface waves (Smith et al., 2023). Recent studies also suggest that attenuation parameters can be extracted from ambient noise data (Li et al., 2020). When combined with forward modeling techniques, this approach can significantly enhance constraints on subsurface material properties. However, accurately computing phase velocities and the overall attenuation factor on surface wave in attenuating media is challenging, as root-finding algorithms used in

elastic case must be extended to the complex domain. These methods require precise initial guesses and are susceptible to numerical instabilities and root omission, particularly during cases of mode kissing (Orta et al., 2022). In contrast, eigenvalue-based approaches that solve linear systems directly (Park, 1996) offer a more robust and stable alternative, avoiding issues related to missing roots.

Sensitivity kernels that link observed dispersion to subsurface model parameters are crucial for seismic inversion. One of the most common approaches to compute these kernels is based on Rayleigh's principle, which relies on the Virial theorem stating that the time-averaged kinetic and potential energies are equal in elastic media (Aki and Richards, 2002). However, this method has an important limitations that it is only valid in elastic media, as the Virial theorem does not hold in viscoelastic media. Therefore, most studies on the derivation of attenuation factors from surface waves rely on perturbation theory based on an elastic background medium (Aki and Richards, 2002), which is only valid under the assumption of weak attenuation. While the dual Lagrangian formulation (Ben-Menahem and Singh, 2012) has been proposed to address this issue, it is restricted to computing derivatives of eigenvalues (i.e., phase velocities). Extending this framework to derived quantities such as group velocities is challenging, as it requires first-order perturbations of the energy integrals (Aki and Richards, 2002; Haney and Tsai, 2017). Another approach is the to compute derivatives directly on the propagation matrices (Hu and Zhu, 2018). However, it is constrained to stratified media and requires a large number of thin layers to accurately represent smoothly varying structures. In contrast, adjoint methods (Tromp et al., 2005; Liu and Tromp, 2008) provide a robust and flexible framework for sensitivity analysis in complex PDE-based constraints. These methods have recently been applied to surface wave dispersion studies (Hawkins, 2018), yet a comprehensive adjoint formulation for anisotropic, attenuating media remains underdeveloped.

This paper is organized as follows. First, we briefly present the theory of surface wave computation using the spectral element method (SEM). We then describe the discretization strategy and the integration of various physical phenomena—anisotropy, attenuation, and acoustic-viscoelastic coupling—into the SEM framework. Next, we discuss the adjoint method and its application for computing derivatives of any quantity with respect to arbitrary parameters. Finally, we present three numerical examples that demonstrate the accuracy and potential of our approach.

THEORY

We start with the source-free anisotropic (visco)elastic wave equation in the frequency domain (Aki and Richards, 2002):

$$-\omega^2 \rho u_i = \sigma_{ij,j}$$

$$\sigma_{ij} = c_{ijkl} u_{k,l}$$
(1)

where ρ is the density and c_{ijkl} represents the fourth-order (visco)elastic tensor that relate stress response and the strain within the material, u_i is the displacement, σ_{ij} is the stress tensor and ω is the angular frequency. Throughout this paper, the indices i, j, k, l range from 1 to 3 and are used to represent the spatial directions x, y, z. Unless explicitly stated otherwise, we follow the Einstein summation convention, where any index that appears twice in a single term implies a summation over its range. In 1-D model (Figure 1), we seek to find the homogeneous plane wave solution to equation (1) with the ansatz (Dahlen and Tromp, 1998; Aki and Richards, 2002):

$$u_i(\mathbf{r}, z, \omega) = U_i(z, \omega) \exp(i\omega t - i\mathbf{k} \cdot \mathbf{r})$$
(2)

where U_i is the polarization vector, \mathbf{r} is the horizontal coordinates, $\mathbf{k} = k\hat{k}$ denote the horizontal wavenumber vector, k is the (complex) magnitude and \hat{k} is the unit direction vector. In this study, only weak attenuation is considered, which only involves a homogeneous plane wave (the real and imaginary parts of the wavenumber vector share the same direction) (Červenỳ and Pšenčík, 2008). Under free surface boundary conditions at the top and radiation boundary conditions at infinity, equation (1) and equation (2) together define an eigenvalue problem that determines the wavenumber k for a given propagation direction \hat{k} and the angular frequency ω . By substituting Eq.(2) into Eq.(1), we derive the eigen-equations ODEs for surface waves:

$$T_{i} = \hat{z}_{j} c_{ijpq} (-ik_{q} U_{p} + \hat{z}_{q} \partial_{z} U_{p}) = \hat{z}_{j} \sigma_{ij}$$

$$\partial_{z} T_{i} - ik_{j} c_{ijpq} (-ik_{q} U_{p} + \partial_{z} U_{p} \hat{z}_{q}) + \rho \omega^{2} U_{i} = 0$$
(3)

where \hat{z} is the unit vector along z axis in Figure 1, T_i is the traction σ_{i3} .

Another important factor influencing surface wave dispersion is the presence of fluid layers (Kugler et al., 2007), particularly in marine seismology, where the effect of the fluid cannot be neglected at high frequencies (Wang et al., 2016). To account for the influence of the fluid, the frequency-domain acoustic wave equation (Chaljub et al., 2007; Bottero et al., 2016) must also be modeled within the water column as:

$$-\omega^2 \kappa^{-1} \chi = (-ik_i U_i + \partial_z U_i \hat{z}_i)$$

$$U_i = \rho^{-1} (-ik_i \chi + \partial_z \chi \hat{z}_i)$$
(4)

here κ is the bulk modulus and χ is the scalar potential in acoustic material which is related to pressure as :

$$P = \omega^2 \chi \tag{5}$$

At elastic-fluid boundaries, the coupling condition is:

$$T_{z} = \hat{z}_{i} T_{i} = -P = -\omega^{2} \chi$$

$$T_{k} = \hat{k}_{i} T_{i} = 0$$

$$[u_{z}]_{-}^{+} = [u_{i} \hat{z}_{i}]_{-}^{+} = 0$$
(6)

And the free surface $(z=z_0)$ and radiation boundary condition $(z\to\infty)$ are applied as:

$$T_i|_{z\to\infty} = 0; \quad \chi|_{z=z_0} = 0; \quad T_i|_{z=z_0} = 0$$
 (7)

The eigenvalues can be determined using various numerical methods. In this paper, we apply the spectral element method (SEM) (Hawkins, 2018; Shi et al., 2022) to solve this eigenvalue problem. Consequently, we adopt the weak form of the wave equation:

$$-\omega^{2} \int_{0}^{\infty} \rho U_{i} \psi \, dz = -ik_{j} \int_{0}^{\infty} c_{ijpq} (-ik_{q}U_{p} + \partial_{z}U_{p}\hat{z}_{q}) \psi \, dz$$

$$- \int_{0}^{\infty} T_{i} \partial_{z} \psi \, dz \pm \omega^{2} \sum_{n=1}^{N_{cs}} [\chi \psi]_{z_{n}}$$

$$-\omega^{2} \int_{0}^{\infty} \kappa^{-1} \chi \psi dz = -k^{2} \int_{0}^{\infty} \rho^{-1} \chi \psi dz - \int_{0}^{\infty} \rho^{-1} \partial_{z} \chi \partial_{z} \psi \, dz$$

$$\pm \sum_{n=1}^{N_{cs}} [U_{3} \psi]_{z_{n}}$$
(8)

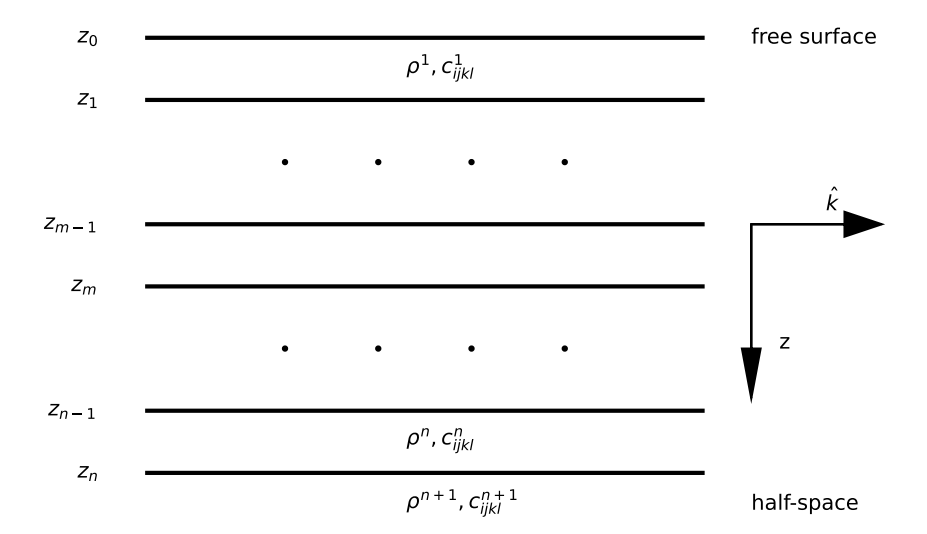


Figure 1: Diagram of 1D anisotropic model. \hat{k} is the direction of wavenumber vector.

Here, ψ denotes the trial function, and N_{cs} represents the number of fluid-elastic coupling surfaces. The sign \pm is determined by the relative position of the elastic and acoustic materials, depending on which side each material is located.

METHOD

Discretization

In SEM framework, the study region is discretized into a set of non-overlapping elements (Komatitsch and Tromp, 1999). Within each element, the wavefield and elastic parameters are approximated using Lagrangian interpolation on given quadrature-dependent nodes. Discountinuities and multiphysics coupling surface is honored by

element boundaries.

The study region in this work includes both a finite domain and a half-infinite domain, necessitating different quadrature rules. For the finite domain, Gauss-Legendre-Lobatto (GLL) nodes are employed, as they provide near-optimal interpolation accuracy in practice (Hesthaven, 1998). For the half-infinite domain, we utilize Gauss-Radau-Legendre (GRL) quadrature, which is well-suited for evaluating integrals in unbounded spaces. This combination of GLL and GRL quadrature has been successfully applied in other applications, such as the simulation of gravity anomalies (Gharti et al., 2018). Therefore, in each element, we can approximate the wavefield and elastic parameters as:

$$U_{i} = \sum_{p=1}^{n} U_{i}^{p} l_{p}(\xi); \ \rho = \sum_{p=1}^{n} \rho^{p} l_{p}(\xi); \ c_{ijkl} = \sum_{p=1}^{n} c_{ijkl}^{p} l_{p}(\xi)$$
 (9)

Here, $l_p(\xi)$ represents the p-th Lagrange interpolant, $U_i^p = U_i(\xi_p)$, and ξ denotes the local coordinates obtained by mapping the original interval to the interval required by the quadrature rules. Since the SEM is a Bubnov–Galerkin type method, the trial functions are chosen as the same set of interpolants (Komatitsch and Tromp, 1999). By inserting equation (9) into the weak form equations (8), we can finally reorganize it to a quadratic eigenvalue problem of k:

$$\omega^2 M x = k^2 K x + k H x + E x \tag{10}$$

Where $\boldsymbol{x} = (U_1, U_2, U_3, \chi)^T$ represents the three components of displacement \boldsymbol{U} , the scalar potential χ and $\boldsymbol{M}, \boldsymbol{K}, \boldsymbol{H}, \boldsymbol{E}$ are matrices through global assembly. This problem can be addressed by transforming it into a generalized eigenvalue problem (Tisseur and Meerbergen (2001), also in Appendix B). The resulting eigenvalue problem can

then be efficiently solved using Schur decomposition, a method that has been widely implemented in various mathematical libraries, such as Intel MKL and OpenBLAS. After we obtaining k, the (complex) phase velocity c can be obtained directly by $c = \omega/k$. For weakly anelastic medium, we can define the quality factor and the propagation phase velocity as:

$$\tilde{c} := \omega/k = c\left(1 + \frac{i}{2Q_c}\right) \tag{11}$$

where c and Q_c are real-valued quantities representing the propagation phase velocity and the quality factor associated with the phase velocity, respectively.

Radial Anisotropy

A practically relevant special case arises when the material exhibits radial anisotropy, also known as vertical transverse isotropy (VTI). In this scenario, Rayleigh and Love waves are separable, and coupling between the fluid and elastic wavefield only needs to be considered for the Rayleigh wave (also known as Scholte wave). Additionally, the phase velocity $c(\omega)$ is not dependent on the azimuthal angles. Therefore, we can solve this problem by dividing them into two subproblems. By introducing a transformation

$$\bar{U}_3 = ikU_3; \ \bar{\chi} = ik\chi \tag{12}$$

that can eliminate the first order of k in equation (10) and make all eigenfunctions be in real numbers, which save memory cost for eigenvalue problem. By inserting the VTI model c_{ijkl} expressions:

$$c_{ijkl} = (A - 2N)\delta_{ij}\delta_{kl} + N(\delta_{ik}\delta_{jl} + \delta_{il}\delta_{jk})$$

$$+ (F - A + 2N)(\delta_{ij}\hat{z}_k\hat{z}_l + \delta_{kl}\hat{z}_i\hat{z}_j)$$

$$+ (L - N)(\delta_{ik}\hat{z}_j\hat{z}_l + \delta_{il}\hat{z}_j\hat{z}_k + \delta_{jk}\hat{z}_i\hat{z}_l + \delta_{jl}\hat{z}_i\hat{z}_k)$$

$$+ (A + C - 2F - 4L)\hat{z}_i\hat{z}_j\hat{z}_k\hat{z}_l$$

$$(13)$$

here \hat{z} is the z axis direction in Figure 1, δ_{ij} is Kronecker delta symbol. The Love parameters A, C, L, F, N are defined by using several characteristic velocities:

$$A = \rho \alpha_h^2, \quad C = \rho \alpha_v^2, \quad N = \rho \beta_h^2$$

$$L = \rho \beta_v^2, \quad F = \eta (A - 2L);$$
(14)

where α_h and β_h denote the horizontally polarized P- and S-wave velocities, respectively, and α_v and β_v represent the vertically polarized P- and S-wave velocities along the z-axis. Then we can obtain simplified eigenvalue problem for Love wave as:

$$\omega^2 M x = E x + k^2 K x \tag{15}$$

And for Rayleigh/Scholte wave:

$$\omega^{2} \begin{bmatrix} \mathbf{M} & & \\ & \mathbf{M} & \\ & & \mathbf{M}' \end{bmatrix} \begin{bmatrix} U_{1} \\ \overline{U}_{3} \\ \bar{\chi} \end{bmatrix} = k^{2} \begin{bmatrix} \mathbf{K}^{1} & \mathbf{0} & \mathbf{0} \\ \mathbf{K}^{2} & \mathbf{K}^{3} & \mathbf{0} \\ \mathbf{0} & \mathbf{0} & \mathbf{K}^{5} \end{bmatrix} \begin{bmatrix} U_{1} \\ \overline{U}_{3} \\ \bar{\chi} \end{bmatrix} + \begin{bmatrix} \mathbf{E}^{1} & \mathbf{E}^{2} & \mathbf{0} \\ \mathbf{0} & \mathbf{E}^{3} & \mathbf{E}^{4} \\ \mathbf{0} & \mathbf{E}^{5} & \mathbf{E}^{6} \end{bmatrix} \begin{bmatrix} U_{1} \\ \overline{U}_{3} \\ \bar{\chi} \end{bmatrix}$$

$$(16)$$

The expressions for each element can be find in Appendix A.

General Anisotropy

For general anisotropic models, the phase velocity depends on the horizontal propagation direction, expressed as $c = c(\omega, \hat{k})$ (Tromp, 1994). In such cases, Rayleigh and Love waves are no longer separable, requiring us to begin with equation (8):

$$\int \rho \omega^2 u_i \psi \, dz = \int ik \left[c_{ijpq} (-ik\hat{k}_j \hat{k}_q u_p + \hat{z}_q \dot{u}_p \hat{k}_j) \right] \psi \, dz +$$

$$\int \left[c_{i3pq} (-ik\hat{k}_q u_p + \hat{z}_q \dot{u}_p) \right] \partial_z \psi \, dz$$
(17)

It is important to note that above equation involves four distinct types of integrals, each of which can be computed by using Gaussian quadrature:

$$\int_{\Omega_{k}} PU\psi \ dz = \sum_{j} w_{i} P_{i} J_{k} \delta_{ij} U_{j}$$

$$\int_{\Omega_{k}} P\partial_{z} U\psi \ dz = \sum_{j} w_{i} P_{i} l'_{j}(\xi_{i}) U_{j}$$

$$\int_{\Omega_{k}} PU\partial_{z} \psi \ dz = \sum_{j} w_{j} P_{j} l'_{i}(\xi_{j}) U_{j}$$

$$\int_{\Omega_{k}} P\partial_{z} U\partial_{z} \psi \ dz = J_{k}^{-1} \sum_{j} \sum_{m} w_{m} P_{m} l'_{j}(\xi_{m}) l'_{i}(\xi_{m}) U_{j}$$
(18)

Here P denotes the physical parameters such as rho or c_{ijkl} , and U is the eigenfunction to solve, w_i is the i-th quadrature weights, and $J_k = \mathrm{d}z/\mathrm{d}\xi$ is the Jacobian in k-th element. Variables with subscript i, j, such as U_j are abbreviate of $U(\xi_j)$. Finally we can obtain the quadratic eigenvalue problem as equation (10), and the element matrices can be found in Appendix A.

Attenuation

In attenuating medium, the strain-stress relation is through Boltzmann's superposition principle (Carcione, 1990)

$$\sigma_{ij}(t) = \int_0^t d\tau \ c_{ijkl}(t-\tau)\partial_\tau \epsilon_{kl}(\tau)$$
 (19)

We can approximate the attenuation effects using a series of standard linear solids (Aki and Richards, 2002). In this assumption, the anelastic tensor c_{ijkl} is (Komatitsch and Tromp, 1999):

$$c_{ijkl}(t) = c_{ijkl}^R \left[1 + \sum_{p=1}^N \tau_{ijkl}^p e^{-\omega_p t} \right] H(t),$$
 (20)

where c_{ijkl}^R denotes the relaxed elastic tensor $(\lim_{t\to\infty} c_{ijkl}(t))$, H(t) is the Heaviside function, N is the number of standard linear solids used, and ω_p , τ_{ijkl}^p are the stress relaxation frequency and a attenuation-related factor for p-th standard linear solid, respectively. By Fourier transform, we can find the frequency domain expressions as:

$$\sigma_{ij}(\omega) = c_{ijkl}^R \left[1 + \sum_{p=1}^N \frac{i\omega \tau_{ijkl}^p}{\omega_p + i\omega} \right] \epsilon_{kl}(\omega) = M_{ijkl}(\omega) \epsilon_{kl}(\omega)$$
 (21)

The definition of quality factor Q^{-1} is (Dahlen and Tromp, 1998; Aki and Richards, 2002):

$$Q_{ijkl}^{-1}(\omega) = \frac{\text{Im} M_{ijkl}}{\text{Re} M_{ijkl}} = \frac{\sum_{p} \tau_{ijkl}^{p} \frac{\omega/\omega_{p}}{1 + (\omega/\omega_{p})^{2}}}{1 + \sum_{p} \tau_{ijkl}^{p} \frac{(\omega/\omega_{p})^{2}}{1 + (\omega/\omega_{p})^{2}}}.$$
 (22)

In the frequency band used in seismology, the quality factor Q is nearly constant, so the parameters ω_p and τ^p_{ijkl} are determined by solving a nonlinear inverse problem that fits a given Q model, such as a constant Q or a power-law model. However, this approach necessitates solving a nonlinear inverse problem for each distinct value of Q in the 1-D model, and it also poses challenges for computing the derivatives of Q. To solve these two issues, Blanch et al. (1995) suggesting selecting ω_p using logarithmic spacing within the frequency range of interest and employing a single τ_{ijkl} for all standard linear solids. This approach allows for the use of an analytical τ -method to determine the optimal parameters efficiently. But this will lead to under-estimated when Q < 20. To address this problem, we adopt the correction approach proposed by van Driel and Nissen-Meyer (2014), which aims to determine the optima ω_p and τ_{ijkl}^p only based on the numerator of equation (22) for a reference quality factor Q_r using the simulated annealing method, then an iterative correction formula is then applied to update τ_{ijkl}^p for other target Q values:

$$\delta_{1} = 1 + \frac{1}{2}\tau_{1}\frac{Q_{r}}{Q}$$

$$\delta_{n+1} = \delta_{n} + \left(\delta_{n} - \frac{1}{2}\right)\tau^{n}\frac{Q_{r}}{Q} + \tau^{n+1}\frac{Q_{r}}{2Q}$$

$$(\tau^{p})' = \delta_{p} \cdot \tau_{p}\frac{Q_{r}}{Q}$$

$$(23)$$

where δ_p is the correction factor for p-th SLS, Q_r is the reference quality factor used for the nonlinear inversion and Q is the target quality factor. This approach significantly reduces the computational cost, as it requires solving only a single nonlinear inverse problem to estimate these parameters. Additionally, it enables direct and efficient derivative computation for Q.

In practice, determining and inverting 21 constant quality factors within the seismic frequency band, along with their corresponding standard linear solid (SLS) models, is challenging (Carcione, 1992). Therefore, in this study, we adopt a simplified approach by selecting only four quality factors for VTI media (Zhu and Tsvankin,

2006), affecting the complex modulus of A, C, L, N. For a general anisotropic model, Carcione and Cavallini (1995) introduces up to four quality factors: one associated with dilatational deformations and three for deviatoric deformations, which should be chosen based on the symmetry of the anisotropic model. The construction of such models on a case-by-case basis is beyond the scope of this study, as our focus is on incorporating attenuation effects and sensitivity analysis into the SEM framework. However, an API can be provided within the SEM code, allowing users to define their own anisotropic attenuating quality factors.

Group Velocity

VTI Model

Another important feature of surface wave observations is the group velocity. For Love wave in radially anisotropic viscoelastic media, we begin with equation (15). Using a perturbation approach, we obtain:

$$2\omega\delta\omega \mathbf{M}\mathbf{x} - \delta\omega \ \partial_{\omega}\mathbf{E}\mathbf{x} + (\omega^{2}\mathbf{M} - \mathbf{E} - k^{2}\mathbf{K})\delta\mathbf{x} = 2k \ \delta k \ \mathbf{K}\mathbf{x}$$
 (24)

To eliminate the term that involves δx , we multiply both sides by the left-hand eigenvector y, resulting in:

$$U_{L,R}^{a,e} = \frac{\partial \omega}{\partial k} = \frac{\mathbf{y}^{\dagger} \mathbf{K} \mathbf{x}}{\mathbf{y}^{\dagger} \left[c \mathbf{M} - (2k)^{-1} \partial_{\omega} \mathbf{E} \right] \mathbf{x}}$$
(25)

where the superscripts e and a stands for elastic and anelastic cases. It should be noted the term $\partial_{\omega} \mathbf{E}$ is nonzero only at fluid-elastic boundaries. This expression is

valid for both Love and Rayleigh waves, and applies to both elastic and anelastic cases. However, the specific form of the eigenvectors and matrices involved can lead to further simplifications depending on the wave type and material symmetry. Specifically, for Love waves, all matrices are symmetric, and thus $\mathbf{y} = \mathbf{x}$ in the elastic case or $\mathbf{y} = \mathbf{x}^*$ in the visco-elastic case. Moreover, the fluid does not affect the dispersion of Love waves. Altogether, these facts lead to:

$$U_L^{e,a} = \frac{\boldsymbol{x}^T \boldsymbol{K} \boldsymbol{x}}{c \ \boldsymbol{x}^T \boldsymbol{M} \boldsymbol{x}} \tag{26}$$

For Rayleigh waves, as we introduced the transformation (12) to avoid solving quadratic eigenvalue problem, the new matrix system is not self-adjoint, so the left and right eigenvectors are generally distinct, yielding:

$$U_R^e = \frac{\boldsymbol{y}^T \boldsymbol{K} \boldsymbol{x}}{\boldsymbol{y}^T \left[c \boldsymbol{M} - (2k)^{-1} \partial_\omega \boldsymbol{E} \right] \boldsymbol{x}}; \quad U_R^a = \frac{\boldsymbol{y}^\dagger \boldsymbol{K} \boldsymbol{x}}{\boldsymbol{y}^\dagger \left[c \boldsymbol{M} - (2k)^{-1} \partial_\omega \boldsymbol{E} \right] \boldsymbol{x}}$$
(27)

General Anisotropy

In this case we should start with variation of equation (10):

$$0 = 2\omega \delta \omega \mathbf{M} \mathbf{x} + (\omega^2 \mathbf{M} - k^2 \mathbf{K} - k \mathbf{H} - \mathbf{E}) \delta \mathbf{x}$$
$$- \delta \omega \ \partial_{\omega} \mathbf{E} - \partial_{k_i} (k^2 \mathbf{K} + k \mathbf{H}) \mathbf{x} \delta k_i$$
(28)

In this case, all eigenvectors are complex, so we multiply with the left eigenvector y^{\dagger} :

$$0 = \boldsymbol{y}^{\dagger} \left(-2\omega \boldsymbol{M} + \partial_{\omega} \boldsymbol{E} \right) \boldsymbol{x} \, \delta\omega + \boldsymbol{y}^{\dagger} \partial_{k_{i}} (k^{2} \boldsymbol{K} + k \boldsymbol{H}) \boldsymbol{x} \delta k_{i}$$
 (29)

note $k^2 \mathbf{K}$ and $k \mathbf{H}$ are quadratic and linear form of vector \mathbf{k} (equation (17)), so we can obtain:

$$U_{i}^{a,e} = \partial \omega / \partial k_{i} = \frac{\mathbf{y}^{\dagger} (k \partial_{\hat{k}_{i}} \mathbf{K} + \partial_{\hat{k}_{i}} \mathbf{H}) \mathbf{x} \delta \hat{k}_{i}}{\mathbf{y}^{\dagger} \left[2\omega \mathbf{M} - \partial_{\omega} \mathbf{E} \right] \mathbf{x}}$$
(30)

For elastic solid media, all matrices are Hermitian (see proof in Appendix D), so:

$$U_{i}^{e,solid} = \partial \omega / \partial k_{i} = \partial \omega / \partial k_{i} = \frac{\boldsymbol{x}^{\dagger} (k \partial_{\hat{k}_{i}} \boldsymbol{K} + \partial_{\hat{k}_{i}} \boldsymbol{H}) \boldsymbol{x} \delta \hat{k}_{i}}{\boldsymbol{x}^{\dagger} \left[2\omega \boldsymbol{M} - \partial_{\omega} \boldsymbol{E} \right] \boldsymbol{x}}$$
(31)

Numerical Implementation

The efficiency and accuracy of the spectral element method (SEM) depend strongly on the choice of element size and the order of Lagrange polynomials for a given frequency and model. Additionally, the discretization of the study region must capture all discontinuities, such as fluid-elastic interfaces. To account for this, we divide the model into multiple regions, ensuring that discontinuities are properly represented. Within each region, material properties can either remain constant or be approximated using linear interpolation. To reduce numerical dispersion the number of GLL points is typically chosen as ≥ 5 (Komatitsch and Tromp, 1999; Lyu et al., 2020), and the element size is generally set to approximately one wavelength at the target frequency. To ensure sufficient accuracy in our implementation, we use $NGLL \geq 7$ and allocate at least 1.5 elements per wavelength. Furthermore, the SEM mesh is re-discretized for each frequency to maintain accuracy.

Another numerical challenge is handling the half-space. The GRL quadrature allows for the application of an arbitrary scaling factor to the infinite element. Hawkins (2018) suggested determining the optimal depth based on the maximum sensitivity depth of the analytical solution for the half-space. However, in general viscoelastic anisotropic media, obtaining such a solution is challenging. Therefore, in our implementation, we set the scaling factor as 10–20 wavelengths within the half-space.

Based on our numerical experiments, we choose the number of GRL nodes to be 15–25 in this study.

Note that using a matrix-based eigenvalue solver yields n eigenvalues, where n is the number of points in the system—typically much larger than the number of physically meaningful dispersion relations. These redundant dispersions originate from numerical dispersion effects introduced by discretizing the system, which result in eigenvalues with strong attenuation coefficients (Shi et al., 2022). To filter out these spurious eigenvalues, we impose the conditions that the real part of the phase velocity must be less than the maximum characteristic velocity in the half-space and that $|\Re k| \geq |\Im k|$.

An important consideration in anisotropic media is that phase velocity depends on direction. Therefore, the characteristic velocity of the half-space, used in the spurious eigenvalue filter, should be determined for each direction by solving the body-wave eigenvalue problem of the Christoffel equation (Cerveny, 2001):

$$\Gamma_{ik}g_k = v^2g_i \tag{32}$$

where $\Gamma_{ik} = c_{ijkl}/\rho \ \hat{n}_j \hat{n}_l$ is the Christoffel matrix, g_i is the polarization vector and \hat{n} is the unit vector for the given direction. We choose the minimum and maximum eigenvalue v as the lower and upper limit used in the spurious mode filter.

FRECHÉT KERNELS AND ADJOINT METHOD

The most prominent method to compute derivatives is utilizing the Lagrangian of the system (Al-Attar and Crawford, 2016). For elastic wave, we have:

$$\mathcal{L}^e = \frac{1}{2}\rho \dot{u}_i \dot{u}_i - \frac{1}{2}c_{ijkl}u_{k,l}u_{i,j}$$
(33)

The Virial theorem states that the time and volume integral of this quantity is zero. For visco-elastic medium, the Hamiltonian is not conserved and thus the Virial theorem does not hold, but we can introduce a "mirror" anti-dissipation system, and make the two systems as a whole (see Appendix C), and obtain the dual Lagrangian as:

$$\mathcal{L}^{a} = \rho \dot{u}_{i} \dot{u}_{i}^{+} - C_{ijkl}^{R} u_{k,l} u_{i,j}^{+} - \frac{1}{2} C_{ijkl}^{I}(t) * \dot{u}_{k,l} u_{i,j}^{+} + \frac{1}{2} C_{ijkl}^{I}(-t) * \dot{u}_{k,l}^{+} u_{i,j}$$
(34)

where u^+ is the displacement of anti-dissipation system, * is the time convolution, the definition of C^R and C^I can be found in Appendix C. Then by applying Rayleigh's principle (Dahlen and Tromp, 1998) we can find the derivatives of phase velocity with respect to any model parameters.

Although this method is elegant, it introduces difficulties when we need to compute complex derivatives for user-defined quantities. So in this study, we will seek to find a general adjoint method (Tromp et al., 2005; Liu and Tromp, 2006) to find all required derivatives.

We start from quadratic eigenvalue problem in equation (10), and let the quantity we want to find derivatives relative to model parameters m as f, Then by Lagrange multiplier method, we can define an auxiliary function as:

$$S = f - \lambda^{\dagger} (\mathbf{A} \mathbf{x} - \alpha \mathbf{B} \mathbf{x}) - \mathbf{x}^{\dagger} (\mathbf{A}^{\dagger} - \alpha^{*} \mathbf{B}^{\dagger}) \boldsymbol{\mu} - s(\mathbf{x}^{\dagger} \mathbf{x} - 1)$$

$$- \mathbf{y}^{\dagger} (\mathbf{A} - \alpha \mathbf{B}) \boldsymbol{\xi} - \boldsymbol{\eta}^{\dagger} (\mathbf{A}^{\dagger} - \alpha^{*} \mathbf{B}^{\dagger}) \mathbf{y} - t(\mathbf{y}^{\dagger} \mathbf{y} - 1)$$
(35)

where α is the eigenvalue in the system $(k \text{ or } k^2)$, † stands for the conjugate transpose, \boldsymbol{A} and \boldsymbol{B} are matrices for which the eigenvalues are to be computed, \boldsymbol{x} and \boldsymbol{y} are right and left eigenvectors, respectively, and $\boldsymbol{\lambda}, \boldsymbol{\mu}, \boldsymbol{\xi}, \boldsymbol{\eta}, s, t$ are Lagrange multipliers. Then variation of \mathcal{S} according to small variation of model parameters $\delta \boldsymbol{m}$ is:

$$\delta S = \left[\frac{\partial f}{\partial x_{i}} - \lambda_{j}^{*} (A_{ji} - \alpha B_{ji}) - s x_{i}^{*} \right] \delta x_{i} + \left[\frac{\partial f}{\partial x_{i}^{*}} - (A_{ji}^{*} - \alpha^{*} B_{ji}^{*}) \mu_{j} - s x_{i} \right] \delta x_{i}^{*}$$

$$+ \left[\frac{\partial f}{\partial y_{i}^{*}} - (A_{ij} - \alpha B_{ij}) \xi_{j} - t y_{i} \right] \delta y_{i}^{*} + \left[\frac{\partial f}{\partial y_{i}} - \eta_{j}^{*} (A_{ji}^{*} - \alpha B_{ji}^{*}) - t y_{i}^{*} \right] \delta y_{i}$$

$$+ \left[\frac{\partial f}{\partial \alpha} + \boldsymbol{\lambda}^{\dagger} \boldsymbol{B} \boldsymbol{x} + \boldsymbol{y}^{\dagger} \boldsymbol{B} \boldsymbol{\xi} \right] \delta \alpha + \left[\frac{\partial f}{\partial \alpha^{*}} + \boldsymbol{x}^{\dagger} \boldsymbol{B}^{*} \boldsymbol{\mu} + \boldsymbol{\eta}^{\dagger} \boldsymbol{B}^{*} \boldsymbol{y} \right] \delta \alpha^{*}$$

$$- \left[\boldsymbol{\lambda}^{\dagger} (\frac{\partial \boldsymbol{A}}{\partial m_{i}} \boldsymbol{x} - \alpha \frac{\partial \boldsymbol{B}}{\partial m_{i}} \boldsymbol{x}) + \boldsymbol{x}^{\dagger} (\frac{\partial \boldsymbol{A}^{\dagger}}{\partial m_{i}} - \alpha^{*} \frac{\partial \boldsymbol{B}^{\dagger}}{\partial m_{i}}) \boldsymbol{\mu} \right] \delta m_{i}$$

$$- \left[\boldsymbol{y}^{\dagger} (\frac{\partial \boldsymbol{A}}{\partial m_{i}} - \alpha \frac{\partial \boldsymbol{B}}{\partial m_{i}}) \boldsymbol{\xi} + \boldsymbol{\eta}^{\dagger} (\frac{\partial \boldsymbol{A}^{\dagger}}{\partial m_{i}} - \alpha^{*} \frac{\partial \boldsymbol{B}^{\dagger}}{\partial m_{i}}) \boldsymbol{y} \right] \delta m_{i}$$

$$+ \left[\frac{\partial f}{\partial \boldsymbol{A}} : \frac{\partial \boldsymbol{A}}{\partial m_{i}} + \frac{\partial f}{\partial \boldsymbol{B}} : \frac{\partial \boldsymbol{B}}{\partial m_{i}} \right] \delta m_{i}$$

So we can obtain 6 adjoint equations as:

$$\frac{\partial f}{\partial x_{i}} - \lambda_{j}^{*}(A_{ji} - \alpha B_{ji}) - sx_{i}^{*} = 0; \quad \frac{\partial f}{\partial x_{i}^{*}} - (A_{ji}^{*} - \alpha^{*}B_{ji}^{*})\mu_{j} - sx_{i} = 0$$

$$\frac{\partial f}{\partial y_{i}^{*}} - (A_{ij} - \alpha B_{ij})\xi_{j} - ty_{i} = 0; \quad \frac{\partial f}{\partial y_{i}} - \eta_{j}^{*}(A_{ji}^{*} - \alpha B_{ji}^{*}) - ty_{i}^{*} = 0$$

$$\frac{\partial f}{\partial \alpha} + \lambda^{\dagger} \mathbf{B} \mathbf{x} + \mathbf{y}^{\dagger} \mathbf{B} \boldsymbol{\xi} = 0; \quad \frac{\partial f}{\partial \alpha^{*}} + \mathbf{x}^{\dagger} \mathbf{B}^{\dagger} \boldsymbol{\mu} + \boldsymbol{\eta}^{\dagger} \mathbf{B}^{\dagger} \mathbf{y} = 0$$
(37)

by utilizing normalization condition, we can solve s and t as:

$$s = x_i \frac{\partial f}{\partial x_i} = x_i^* \frac{\partial f}{\partial x_i^*}; \quad t = y_i^* \frac{\partial f}{\partial y_i^*} = y_i \frac{\partial f}{\partial y_i}$$
 (38)

However, most quantities we are interested (such as phase velocity, group velocity and HV ratio) is the 0-th order homogeneous function of eigenvector, i.e. $f(c\mathbf{x}) = f(\mathbf{x})$.

Then by using Euler's theorem for homogeneous function, we know both s and t are zero. Then we need to solve 4 linear systems as:

$$(\mathbf{A} - \alpha \mathbf{B})^{\dagger} \boldsymbol{\lambda} = (\partial f / \partial \boldsymbol{x})^{*}; \ (\mathbf{A} - \alpha \mathbf{B})^{\dagger} \boldsymbol{\mu} = \partial f / \partial \boldsymbol{x}^{*}$$

$$(\mathbf{A} - \alpha \mathbf{B}) \boldsymbol{\xi} = \partial f / \partial \boldsymbol{y}^{*}; \ (\mathbf{A} - \alpha \mathbf{B}) \boldsymbol{\eta} = (\partial f / \partial \boldsymbol{y})^{*}$$
(39)

Note that if we have found λ , μ , ξ , η , for any constants c_1 , c_2 , c_3 , c_4 , the $\lambda + c_1 y$, $\mu + c_3 y$, $\xi + c_2 x$, $\eta + c_4 x$ are still valid solutions, so we need another two equations as:

$$\frac{\partial f}{\partial \alpha} + (\boldsymbol{\lambda} + c_1 \boldsymbol{y})^{\dagger} \boldsymbol{B} \boldsymbol{x} + \boldsymbol{y}^{\dagger} \boldsymbol{B} (\boldsymbol{\xi} + c_2 \boldsymbol{x}) = 0;$$

$$\frac{\partial f}{\partial \alpha^*} + \boldsymbol{x}^{\dagger} \boldsymbol{B}^{\dagger} (\boldsymbol{\mu} + c_3 \boldsymbol{y}) + (\boldsymbol{\eta} + c_4 \boldsymbol{x})^{\dagger} \boldsymbol{B}^{\dagger} \boldsymbol{y} = 0$$
(40)

we can find:

$$c_{1}^{*} + c_{2} = -\frac{\partial f/\partial \alpha + \boldsymbol{\lambda}^{\dagger} \boldsymbol{B} \boldsymbol{x} + \boldsymbol{y}^{\dagger} \boldsymbol{B} \boldsymbol{\xi}}{\boldsymbol{y}^{\dagger} \boldsymbol{B} \boldsymbol{x}}$$

$$c_{3} + c_{4}^{*} = -\frac{\partial f/\partial \alpha^{*} + \boldsymbol{x}^{\dagger} \boldsymbol{B}^{\dagger} \boldsymbol{\mu} + \boldsymbol{\eta}^{\dagger} \boldsymbol{B}^{\dagger} \boldsymbol{y}}{\boldsymbol{x}^{\dagger} \boldsymbol{B}^{\dagger} \boldsymbol{y}}$$

$$(41)$$

Insert in equation (37), and also utilize \boldsymbol{A} and \boldsymbol{B} are linear functions of \boldsymbol{m} we can finally obtain:

$$\delta S = -\left[\boldsymbol{\lambda}^{\dagger} \left(\frac{\partial \boldsymbol{A}}{\partial m_{i}} - \alpha \frac{\partial \boldsymbol{B}}{\partial m_{i}}\right) \boldsymbol{x} + \boldsymbol{x}^{\dagger} \left(\frac{\partial \boldsymbol{A}^{\dagger}}{\partial m_{i}} - \alpha^{*} \frac{\partial \boldsymbol{B}^{\dagger}}{\partial m_{i}}\right) \boldsymbol{\mu}\right] \delta m_{i}$$

$$-\left[\boldsymbol{y}^{\dagger} \left(\frac{\partial \boldsymbol{A}}{\partial m_{i}} - \alpha \frac{\partial \boldsymbol{B}}{\partial m_{i}}\right) \boldsymbol{\xi} + \boldsymbol{\eta}^{\dagger} \left(\frac{\partial \boldsymbol{A}^{\dagger}}{\partial m_{i}} - \alpha^{*} \frac{\partial \boldsymbol{B}^{\dagger}}{\partial m_{i}}\right) \boldsymbol{y}\right] \delta m_{i}$$

$$-\left[\left(c_{1}^{*} + c_{2}\right) \boldsymbol{y}^{\dagger} \left(\frac{\partial \boldsymbol{A}}{\partial m_{i}} - \alpha \frac{\partial \boldsymbol{B}}{\partial m_{i}}\right) \boldsymbol{x}\right] \delta m_{i}$$

$$-\left[\left(c_{3} + c_{4}^{*}\right) \boldsymbol{x}^{\dagger} \left(\frac{\partial \boldsymbol{A}^{\dagger}}{\partial m_{i}} - \alpha^{*} \frac{\partial \boldsymbol{B}^{\dagger}}{\partial m_{i}}\right) \boldsymbol{y}\right] \delta m_{i}$$

$$+\left[\frac{\partial f}{\partial \boldsymbol{A}} : \frac{\partial \boldsymbol{A}}{\partial m_{i}} + \frac{\partial f}{\partial \boldsymbol{B}} : \frac{\partial \boldsymbol{B}}{\partial m_{i}}\right] \delta m_{i}$$

$$(42)$$

Another important consideration is the efficient solution of the linear systems in equation (39), which typically entails a computational complexity of $O(n^3)$. However,

this cost can be significantly reduced by exploiting the generalized Schur decomposition of these two matrices:

$$A = QSZ^{\dagger}, B = QS'Z^{\dagger} \tag{43}$$

Here, Q and Z are unitary matrices, and S and S' are upper triangular matrices. This structure enables the linear systems in the adjoint framework to be efficiently solved using forward and backward substitution, reducing the computational complexity to $O(n^2)$. Note that this decomposition was already computed during the computation of eigenvalues and eigenvectors of the system, allowing the four resulting matrices to be cached in memory and reused during sensitivity analysis.

Also note that the adjoint method used in this study depends on the specific discretizations of the ODE system (3), distinguishing it from the approach in Liu and Tromp (2008), which is based on functional analysis. Therefore, it is commonly referred to the discrete adjoint method (Giles et al., 2003).

NUMERICAL EXPERIMENTS

Love Waves in a Two-Layered Anelastic Radially Anisotropic

Medium

One classical example is the two-layer Love wave model, where an analytical dispersion relation can be derived. Following Aki and Richards (2002), the dispersion relation

in this VTI media is given by:

$$F(c) = \frac{L_2}{L_1} \frac{\beta_{v1}}{\beta_{v2}} \frac{\sqrt{\beta_{h2}^2 - c^2}}{\sqrt{c^2 - \beta_{h1}^2}} - \tan\left[\frac{\omega H}{c\beta_{v1}} \sqrt{c^2 - \beta_{h1}^2}\right] = 0$$
 (44)

where H stands for the thickness of the first layer, c is the phase velocity, variables with subscripts 1 and 2 denote parameters in the first and second layers, respectively. After we find the phase velocity, the group velocity is given by:

$$U = c + k \frac{dc}{dk} = \frac{\beta_{h1}^2}{c} \frac{c^2/\beta_{h1}^2 + \Omega}{1 + \Omega}$$
 (45)

where

$$\Omega = \frac{kH\beta_{h2}}{\beta_{v2}} \sqrt{1 - \frac{c^2}{\beta_{h2}^2}} \left[\frac{\rho_1}{\rho_2} \frac{c^2 - \beta_{h1}^2}{\beta_{h2}^2 - \beta_{h1}^2} + \frac{L_2}{L_1} \frac{\beta_{h2}^2 - c^2}{\beta_{h2}^2 - \beta_{h1}^2} \right]$$
(46)

The derivatives can be obtained by:

$$\frac{dc}{dm} = -\frac{\partial F/\partial m}{\partial F/\partial c}; \ \left(\frac{\partial U}{\partial m}\right)_{\omega} = \left(\frac{\partial U}{\partial m}\right)_{\omega c} + \left(\frac{\partial U}{\partial c}\right)_{\omega m} \left(\frac{\partial c}{\partial m}\right)_{\omega} \tag{47}$$

For an elastic model, we can substitute the modulus by using their complex counterpart. Directly solving complex c from equation (44) is error-prone, but we can still analyze the relative error between the true values and the values from SEM by rule of propagation of uncertainty:

$$\left| \frac{\Delta c}{c} \right| \approx \left| \frac{\Delta F}{c \ dF/dc} \right| \tag{48}$$

Table 1 lists all the parameters used in this numerical test. Figure 2 presents a benchmark comparison between the phase and group velocities computed using the SEM and their analytical counterparts over the frequency range of 0.01 Hz to 1 Hz. The results show that the relative error in phase velocity is generally below $10^{-3}\%$,

Table 1: Two-Layer Anelastic VTI Love Wave Model

| Layer Number | h | ρ | β_v | β_h | Q_L | Q_N |
|--------------|----------|-----|-----------|-----------|-------|-------|
| 1 | 35 | 2.8 | 3.0 | 3.3 | 220 | 200 |
| 2 | ∞ | 3.2 | 5.0 | 5.5 | 330 | 300 |

which is practically accurate. Higher-order surface waves exhibit larger errors due to their more oscillatory eigenfunctions, which require higher resolution per wavelength. Figures 3-6 show the comparison of the derivatives of phase and group velocities with respect to model parameters with analytical expressions. We observe that the SEM results coincide perfectly with the analytical solutions. Additionally, for each mode, as frequency increases, the sensitivity gradually shifts toward the first layer. This behavior is consistent with physical intuition, as long-period waves are more sensitive to deeper structures.

Scholte Wave in the Ocean

This example focuses on the propagation of the Scholte wave in the ocean. We set the thickness of the water column to 5 km. To benchmark the results with the matrix method (Haskell, 1990; Dunkin, 1965), we only consider the isotropic media in Table 2, where the ocean bottom is set at the depth of 5 km.

Figure 7 presents the computed phase and group velocities obtained using the

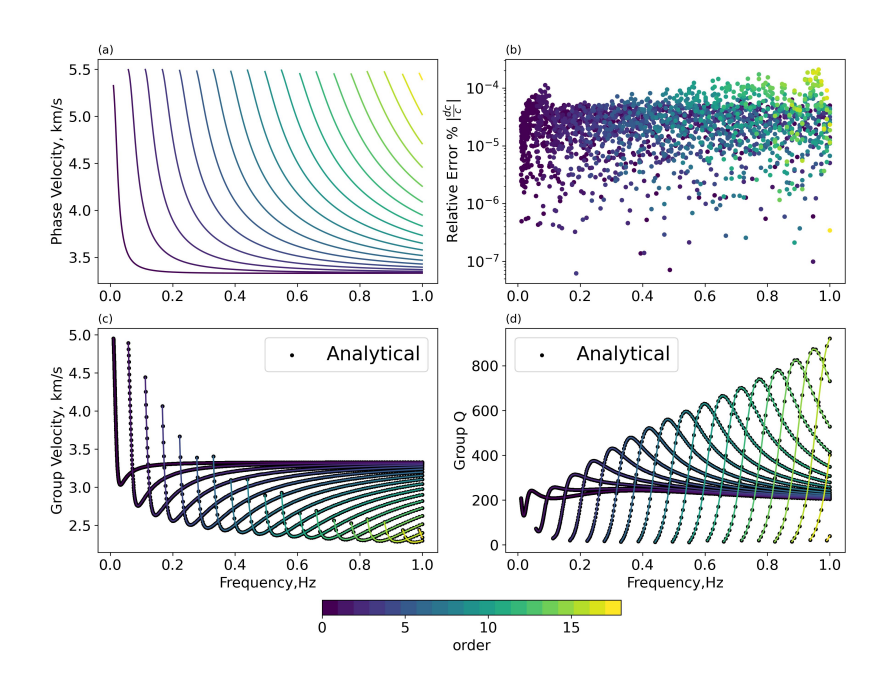


Figure 2: Benchmark on 2-layer Love wave model. Different colors denote different order of surface wave. Dots are from analytical solution. (a) Phase velocity from SEM. (b) Relative error between true eigenvalues and eigenvalues from SEM. (c) Group velocity comparison between SEM and analytical conversion. (d) Group Q value comparison between SEM and analytical conversion

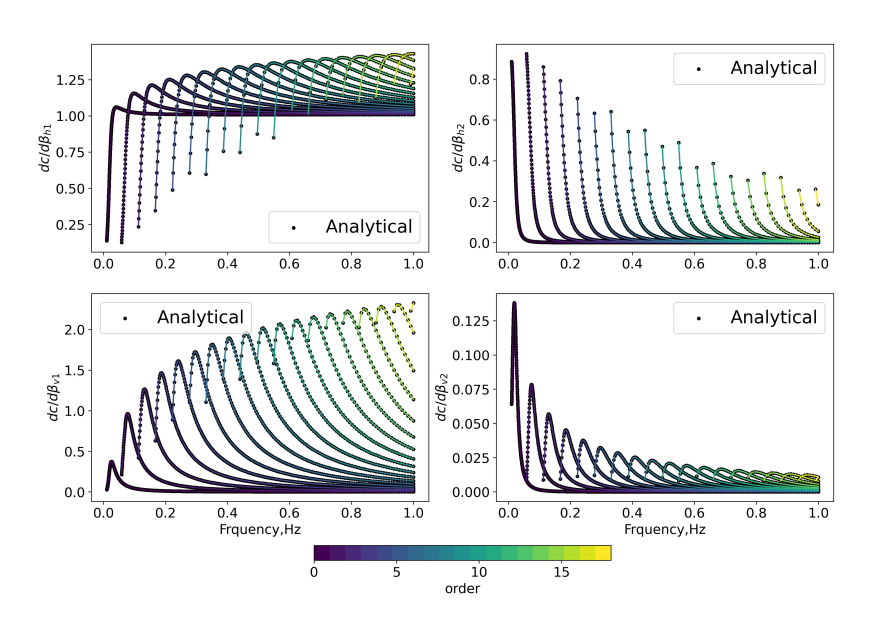


Figure 3: Phase velocity derivatives benchmark on 2-layer Love wave model. Different colors denote different order of surface wave. Dots are from analytical solution. (a),(b),(c),(d) are related to derivatives for β_{h1} , β_{h2} , β_{v1} , β_{v2} , respectively

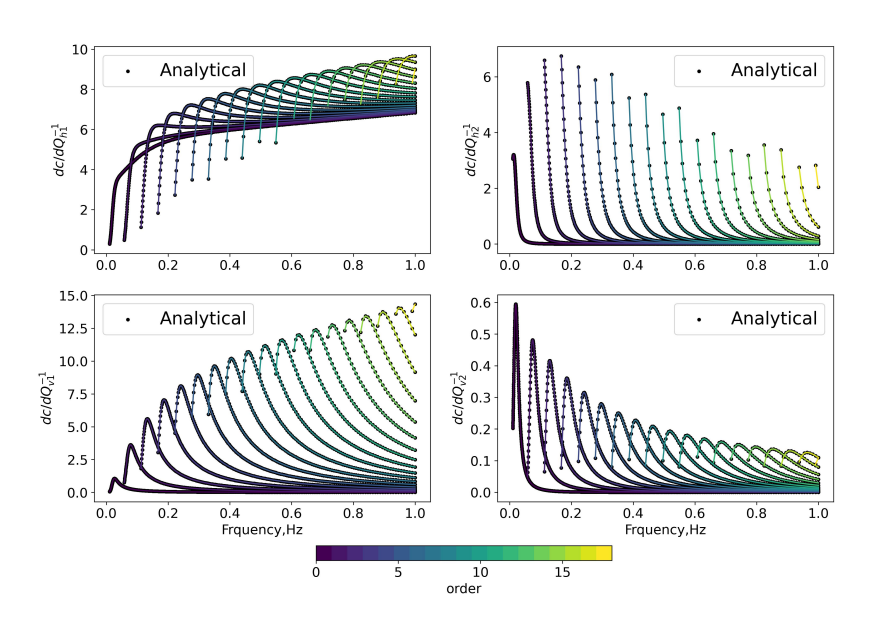


Figure 4: Phase velocity derivatives benchmark on 2-layer Love wave model. Different colors denote different order of surface wave. Dots are from analytical solution. (a),(b),(c),(d) are related to derivatives for $Q_{h1}^{-1}, Q_{h2}^{-1}, Q_{v1}^{-1}, Q_{v2}^{-1}$, respectively

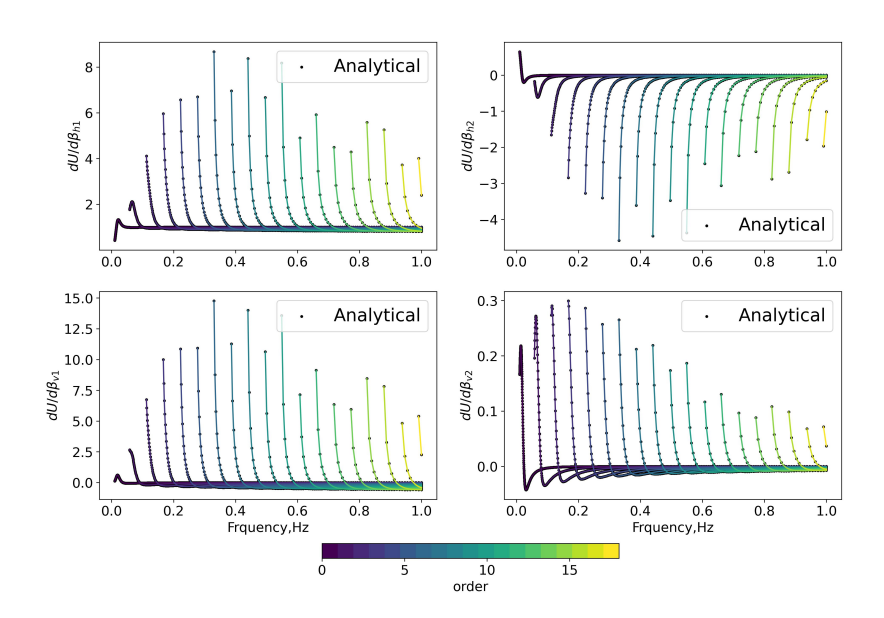


Figure 5: Group velocity derivatives benchmark on 2-layer Love wave model. Different colors denote different order of surface wave. Dots are from analytical solution. (a),(b),(c),(d) are related to derivatives for β_{h1} , β_{h2} , β_{v1} , β_{v2} , respectively

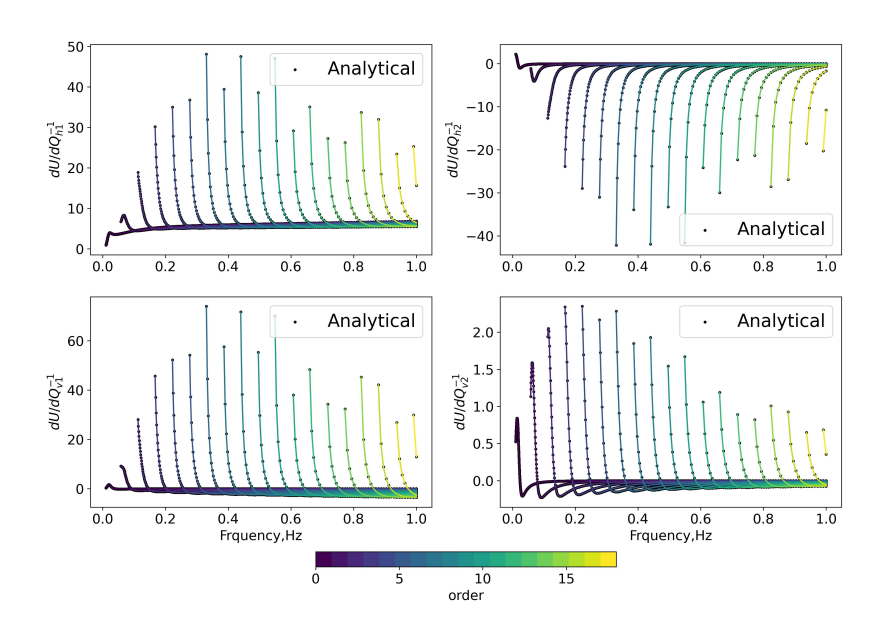


Figure 6: Group velocity derivatives benchmark on 2-layer Love wave model. Different colors denote different order of surface wave. Dots are from analytical solution. (a),(b),(c),(d) are related to derivatives for $Q_{h1}^{-1}, Q_{h2}^{-1}, Q_{v1}^{-1}, Q_{v2}^{-1}$, respectively

Table 2: Four-Layer Elastic Scholte Wave Model

| Layer Number | h | ρ | $\alpha_h = \alpha_v$ | β_v |
|--------------|----------|------|-----------------------|-----------|
| 1 | 5 | 1.03 | 1.5 | 0 |
| 2 | 45 | 2.57 | 5.22 | 3.10 |
| 3 | 50 | 2.95 | 6.94 | 4.0 |
| 4 | ∞ | 3.57 | 5.0 | 8.75 |

spectral element method (SEM) and the matrix method over the frequency range of 0.01 Hz to 0.5 Hz, covering up to six modes. The results from both methods show excellent agreement. Due to the presence of water, mode kissing can be observed at specific frequencies. At higher frequencies, the influence of the fluid becomes increasingly significant. Figure 8 shows the normalized eigen-displacements of the horizontal and vertical components at 0.5 Hz. Notably, at the fluid-solid interface, the tangential displacement is discontinuous across the boundary. For higher modes, the eigenfunctions exhibit increased oscillations and penetrate to greater depths. All displacements decay to zero in the half-space, consistent with the prescribed boundary conditions.

Figures 9–10 present a benchmark comparison of the derivatives of fundamentalmode phase and group velocities with respect to model parameters, obtained using the adjoint method and finite-difference approximations. The results show good

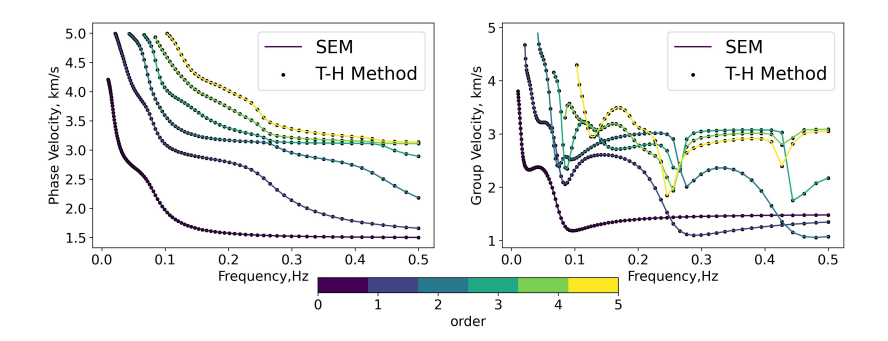


Figure 7: Benchmark of phase/group velocities with SEM and Thompson-Haskell matrix method. Dots in the figure are results from matrix method, and lines are from SEM computation. Only 6 orders has been displayed.

agreement between the two approaches. Additionally, it can also be observed that long-period surface waves exhibit greater sensitivity to deeper structures.

Surface Wave in Orthorhombic Media

Orthorhombic anisotropy is commonly observed in a variety of materials, including fractured reservoirs (Mensch and Farra, 2002), olivine-dominated upper mantle (Keith and Crampin, 1977) and polycrystalline aggregates of ice crystals (Sayers, 2018). The

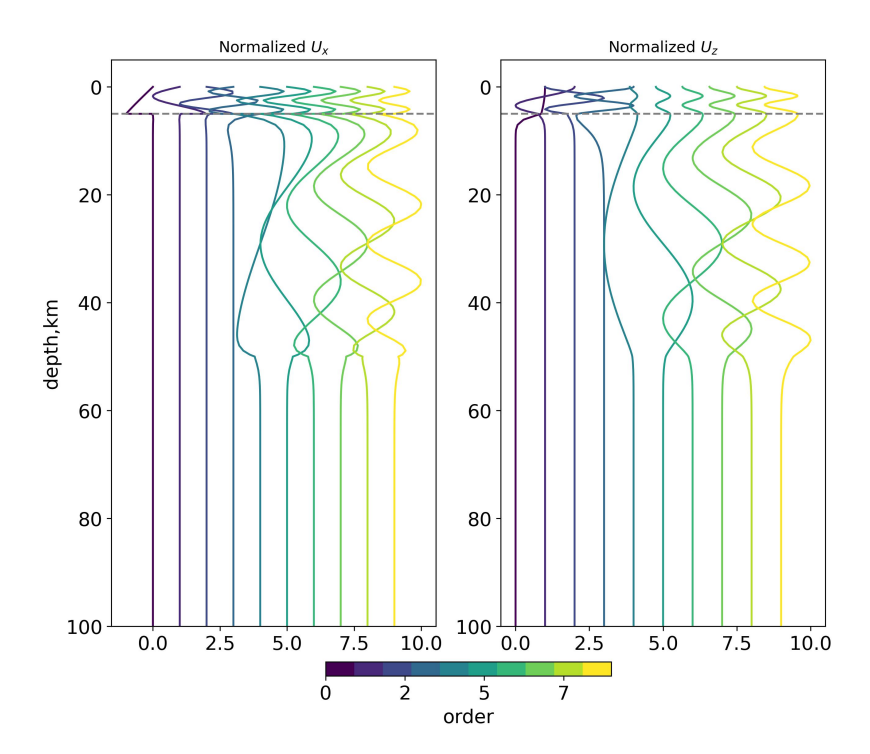


Figure 8: Normalized eigenvectors (displacement) at $0.5 \mathrm{Hz}$ from SEM. We see clearly discontinuities at fluid-elastic boundary (5km depth) on x component

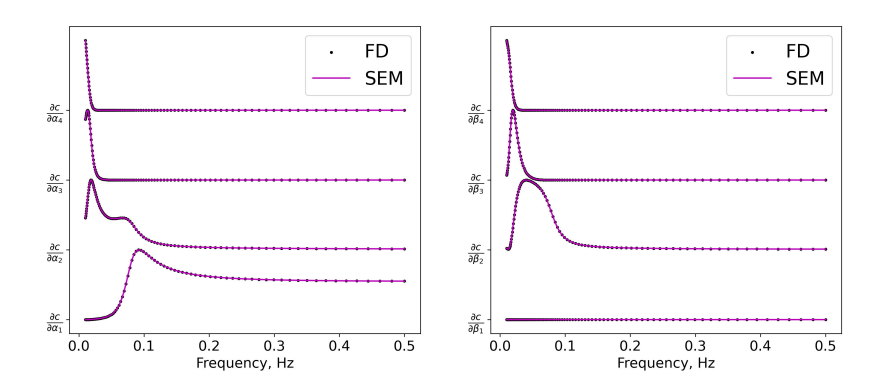


Figure 9: Benchmark of phase velocity derivatives between adjoint method and finite difference approximations. Left: phase velocity derivatives respect to P wave velocities in each layer. Right: phase velocity derivatives respect to S wave velocities in each layer. Only fundamental modes are displayed.

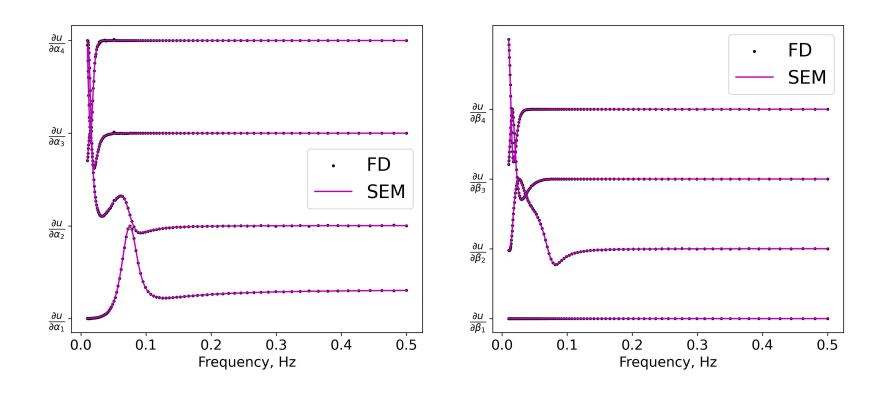


Figure 10: Benchmark of group velocity derivatives between adjoint method and finite difference approximations. Left: group velocity derivatives respect to P wave velocities in each layer. Right: group velocity derivatives respect to S wave velocities in each layer. Only fundamental modes are displayed.

elastic stiffness tensor is expressed in a coordinate-free form as follows (Chevrot, 2006):

$$c_{ijkl} = (C_{13} + C_{23} - C_{12})\delta_{ij}\delta_{kl} + (C_{55} - C_{66} + C_{44})(\delta_{ik}\delta_{jl} + \delta_{il}\delta_{jk})$$

$$+ (C_{12} - C_{23})(a_{i}a_{j}\delta_{kl} + \delta_{ij}a_{k}a_{l}) + (C_{12} - C_{13})(b_{i}b_{j}\delta_{kl} + \delta_{ij}b_{k}b_{l})$$

$$+ (C_{66} - C_{44})(a_{i}a_{k}\delta_{jl} + a_{i}a_{l}\delta_{jk} + a_{j}a_{k}\delta_{il} + a_{j}a_{l}\delta_{ik})$$

$$+ (C_{66} - C_{55})(b_{i}b_{k}\delta_{jl} + b_{i}b_{l}\delta_{jk} + b_{j}b_{k}\delta_{il} + b_{j}b_{l}\delta_{ik})$$

$$+ (C_{11} - C_{13} + C_{23} - C_{12} + 2C_{44} - 2C_{55} - 2C_{66})a_{i}a_{j}a_{k}a_{l}$$

$$+ (C_{22} + C_{13} - C_{23} - C_{12} - 2C_{44} + 2C_{55} - 2C_{66})b_{i}b_{j}b_{k}b_{l}$$

$$+ (C_{33} - C_{13} - C_{23} + C_{12} - 2C_{44} - 2C_{55} + 2C_{66})c_{i}c_{j}c_{k}c_{l}$$

where $\boldsymbol{a}, \boldsymbol{b}, \boldsymbol{c}$ are normal vectors of the three mutually orthogonal planes, and C_{ij} is the elastic tensor in the medium where these normal vectors are parallel to the coordinate system (i.e. $\boldsymbol{a} = \hat{x}, \, \boldsymbol{b} = \hat{y}, \, \boldsymbol{c} = \hat{z}$). We define the attenuation effects only on isotropic compression and shear deformation terms Q_{κ} and Q_{μ} (Carcione, 1990):

$$c'_{II} = c_{II} - \bar{\mathcal{E}} + \bar{K}M_1 + \frac{4}{3}\bar{\mu}M_2, \quad I = 1, 2, 3,$$

$$c'_{IJ} = c_{IJ} - \bar{\mathcal{E}} + \bar{K}M_1 + 2\bar{\mu}\left(1 - \frac{1}{3}M_2\right), \quad I, J = 1, 2, 3; \quad I \neq J,$$

$$c'_{44} = c_{44}M_2, \quad c'_{55} = c_{55}M_2, \quad c'_{66} = c_{66}M_2,$$

$$\bar{\mathcal{E}} = \frac{1}{3}\sum_{I=1}^{3} c_{II}, \quad \bar{\mu} = \frac{1}{3}\sum_{I=4}^{6} c_{II}. \quad \bar{K} = \bar{\mathcal{E}} - \frac{4}{3}\bar{\mu}$$
(50)

where:

$$M_1 = 1 + \sum_{p=1}^{N} \frac{i\omega \tau_{\kappa}^p}{\omega_{\kappa}^p + i\omega}; \quad M_2 = 1 + \sum_{p=1}^{N} \frac{i\omega \tau_{\mu}^p}{\omega_{\mu}^p + i\omega}$$
 (51)

are the SLS approximated complex modulus of the quality factor Q_{κ} and Q_{μ} , c_{ij} is the orthorhombic elastic matrix, and c'_{ij} is the new (an)elastic matrix after including attenuation.

We consider a four-layer model in this example. Each layer shares the same Thomsen-style anisotropic parameters (Tsvankin, 1997), given by: $\epsilon^{(1)} = 0.2$, $\epsilon^{(2)} = 0.1$, $\delta^{(1)} = 0.05$, $\delta^{(2)} = 0.2$, $\delta^{(3)} = -0.1$, $\gamma^{(1)} = 0.15$, and $\gamma^{(2)} = 0.05$. The c-axis orientation is defined by rotation angles $\theta_c = 90^\circ$ and $\phi_c = 45^\circ$. We first focus on a non-dissipative medium; the "isotropic model" parameters, including V_{P0} , V_{S0} , and ρ for each layer, are shown in Figure 11(a). Figure 11(b) shows the phase velocities in the 0.01–0.5 Hz frequency range at an azimuthal angle of 0°. The dispersion curves in Figure 11(b) can be broadly divided into three regions, delineated by three blue lines. These lines correspond to the body wave velocities (2.68, 2.91, and 4.55 km/s, respectively) in the half-space, as derived from equation (32). This segmentation can be interpreted as follows: the existence of surface waves necessitates the presence of inhomogeneous waves (Aki and Richards, 2002), which restricts the phase velocity c to lie between the minimum and maximum characteristic velocities (or the body-wave phase velocities at this direction) of the model.

Figure 12 presents the fundamental mode phase and group velocities at four different azimuthal angles. Since the group velocity does not necessarily align with the phase velocity direction, it is decomposed into two components: u_r , the velocity along the wavenumber direction \hat{k} , and u_t , the component orthogonal to \hat{k} . Prominent azimuthal variations in both phase and group velocities are observed, reflecting strong anisotropic effects. Figure 13 further illustrates the azimuthal dependence of phase and group velocities at 0.05, 0.1, and 0.2 Hz. The phase velocity reaches a maximum at 135° and a minimum at 45°. At these angles, the group velocity (Figure

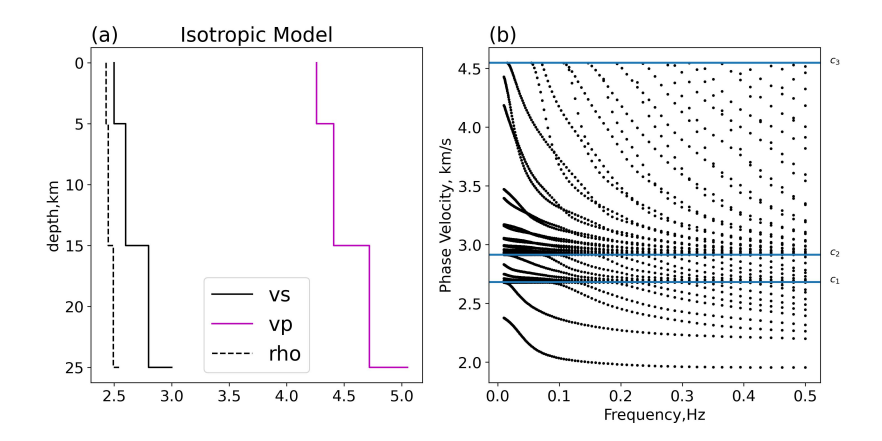


Figure 11: Orthorhombic 1-D model and phase velocities at azimuthal angle = 0°. (a) 4-layer "isotropic model". (b) phase velocities at 0.01 - 0.5 Hz. The 3 horizontal lines are the 3 body-wave phase velocities in half space (2.68, 2.91, and 4.55 km/s, respectively) at current azimuthal angle.

13 (b)) aligns with the phase velocity, consistent with the initial configuration of the anisotropic model. By incorporating attenuation (Figure 14(b)), we observe that the dispersion curves are different from those of the elastic case, particularly for higher modes. This suggests that neglecting attenuation in surface wave inversion could lead to inaccuracies in the resulting model. Figure 15 shows the azimuthal variations of both the phase velocity and the quality factor Q_c , which align with the model configuration, where the slow axis is oriented at 45°. These results indicate that, in attenuating anisotropic media, it is generally possible to constrain the anisotropic model in surface wave inversion by combining the azimuthal variations of both c and Q_c .

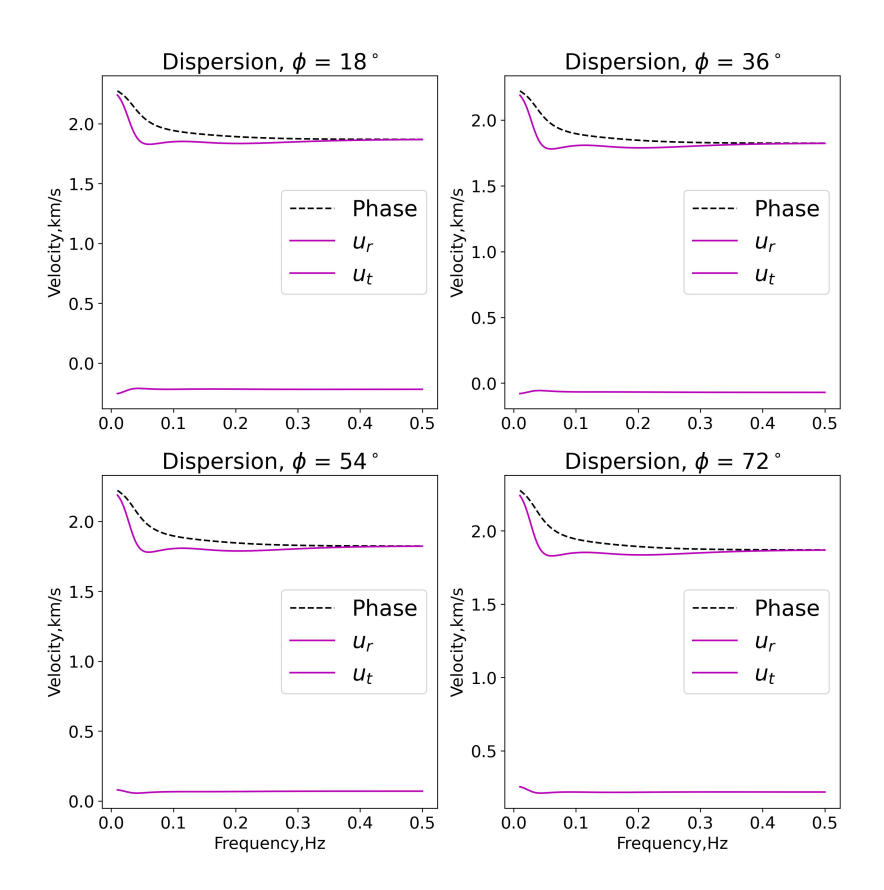


Figure 12: Fundamental mode phase velocities and group velocities at 4 different azimuthal angles. Since the group velocity does not necessarily align with the phase velocity direction, we represent it in terms of components: the velocity along the wavevector \hat{k} direction, u_r , and the orthogonal component, u_t .

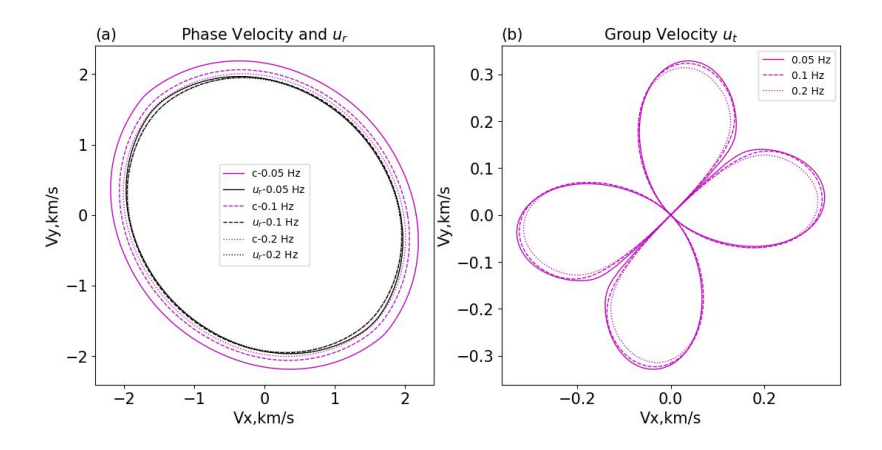


Figure 13: Azimuthal variation of the fundamental mode dispersion for the orthorhombic model. (a) phase velocities and group velocities u_r at 0.05, 0.1, 0.2 Hz. (b) group velocities u_t at 0.05, 0.1, 0.2 Hz

DISCUSSION AND CONCLUSION

This study aims at providing comprehensive and flexible framework based on the spectral element method for modeling 1-D surface wave dispersion and it's derivatives. The framework is capable of simulating elastic, viscoelastic, and multiphysics effects in complex media. To capture attenuation effects, we employ standard linear solid models enhanced with a correction method, resulting in an efficient and differentiable attenuation model. For sensitivity analysis with respect to model parameters, we develop an adjoint method. Through three numerical experiments, the proposed approach demonstrates strong potential for accurately modeling complex dispersion phenomena across various media. In general, this study provides researchers with a powerful and versatile tool for investigating the subsurface structures of the Earth.

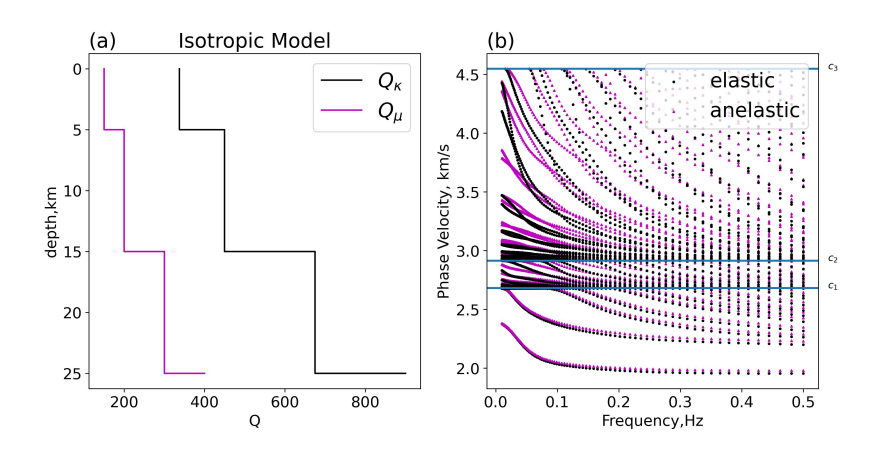


Figure 14: Orthorhombic visco-elastic 1-D model and phase velocities at azimuthal angle = 0°. The "isotropic model" is same as Figure 11. (a) 4-layer "isotropic model". (b) phase velocities at 0.01 - 0.5 Hz. The 3 horizontal lines are the 3 body-wave phase velocities at half space (2.68, 2.91, and 4.55 km/s, respectively) for current azimuthal angle. Black dots are phase velocities for elastic model, and triangulars are phase velocities from visco-elastic model.

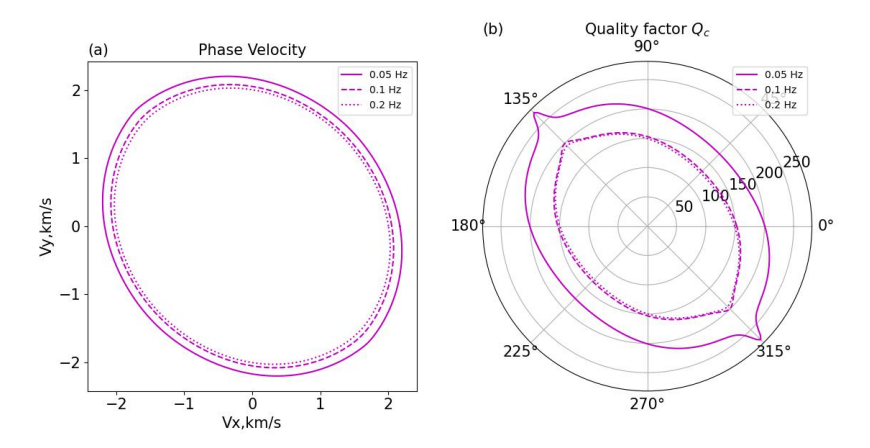


Figure 15: Azimuthal variation of the fundamental mode dispersion for the viscoelastic orthorhombic model. (a) phase velocities at 0.05, 0.1, 0.2 Hz. (b) quality factor Q_c at 0.05, 0.1, 0.2 Hz

Although this framework performs well across all examined topics, there remain opportunities for further work and development based on it.

First, this study is based entirely on flat-layer models, which approximate spherical layering. While the Earth-flattening transformation (Schwab and Knopoff, 1970) can be employed to simulate spherical effects, it becomes inaccurate when complex anisotropy is involved. Moreover, for surface wave propagation over the entire Earth, additional physical effects such as gravity and Earth's rotation must also be incorporated into the forward modeling. This introduces significant complications in both boundary conditions and multiphysics coupling (Tromp, 1994). Even in a simplified scenario where these additional physical effects are neglected, equation (1) must still be reformulated in spherical coordinates, which in turn requires a new discretization

within the SEM framework.

Second, it should be noted that the entire framework presented in this study is applicable only to weakly attenuating media. In strongly attenuating cases, the real and imaginary parts of the wavenumber vector \mathbf{k} may differ significantly (called inhomogeneous waves). Moreover, the attenuation models employed in this work are all based on the simplified constant-Q approximation. More realistic models, such as nearly constant-Q models (Hao and Greenhalgh, 2021), could be adopted in future work, although they require different standard linear solid parameters and alternative approaches for computing derivatives. This extension could be facilitated by providing a user API in the SEM code, allowing users to implement and apply their own attenuation models. Additionally, anisotropic configurations beyond the Love parameters used in the VTI case or the full stiffness tensor \mathbf{C} in the general anisotropic case could be supported through template scripts that handle pre- and post-processing, converting user-supplied models and derivatives into the required internal format.

One of the key applications of surface wave dispersion is surface wave tomography (Shapiro et al., 2005), where ray tracing on 2-D dispersion maps plays a central role. The underlying theory is based on Fermat's principle, which requires the travel time to be stationary with respect to frequency-dependent ray paths (Woodhouse and Wong, 1986):

$$t(\omega) = \int \frac{\hat{k} \cdot \hat{u}}{c(\omega)} \, \mathrm{d}s \tag{52}$$

Here, \hat{k} denotes the unit wavenumber vector, and \hat{u} represents the unit vector in the

direction of group velocity. The term $c(\omega)$ refers to the phase velocity, while ds is the infinitesimal arc length along the surface wave ray path. In isotropic media, \hat{k} and \hat{u} are aligned, and equation (52) simplifies to the well-known result that the ray path of surface waves is solely determined by the phase velocity. However, in the presence of anisotropy, phase and group velocities generally do not share the same direction. Consequently, accurate ray tracing requires knowledge of the azimuthally dependent phase and group velocities at every point along the free surface.

In practice, a widely used method for ray tracing based on equation (52) is the shortest-path method (Zhou and Greenhalgh, 2005), which applies Dijkstra's algorithm to identify the path that minimizes frequency-dependent travel time among all possible trajectories. This approach involves constructing a graph over the 2-D free surface, where each node represents a spatial point with known phase and group velocities in various directions. The travel time between two connected nodes is then computed based on the trapezoidal rule:

$$\Delta t(\boldsymbol{x}_1, \boldsymbol{x}_2) = \frac{1}{2} \left[\frac{\hat{k}(\theta_1) \cdot \hat{u}(\boldsymbol{x}_1, \theta)}{c(\boldsymbol{x}_1, \theta_1)} + \frac{\hat{k}(\theta_2) \cdot \hat{u}(\boldsymbol{x}_2, \theta)}{c(\boldsymbol{x}_2, \theta_2)} \right] |\boldsymbol{x}_i - \boldsymbol{x}_j|$$
 (53)

Here, θ denotes the direction of the straight line connecting two points, while θ_i and θ_j represent the angles at points \boldsymbol{x}_i and \boldsymbol{x}_j , respectively, used to compute the group velocity in the direction of θ . However, determining θ_i directly is not straightforward. In practice, the procedure typically begins with the direction θ , and a local search is conducted within a small angular window around it to identify the angle that yields a group velocity vector most closely aligned with the direction θ .

A notable distinction between surface waves and body waves can be observed from

equation (52). In body wave ray theory, the following identity holds (Cerveny, 2001):

$$\mathbf{s} \cdot \mathbf{u} = 1,\tag{54}$$

where s is the slowness vector and u is the group velocity vector. This identity implies that the projection of the group velocity in the direction of the phase velocity, denoted as u_r , is equal to the phase velocity itself. As a result (from equation (52), the ray path of a body wave is determined solely by its group velocity. However, as illustrated in Figure 13, this identity does not hold for surface waves, since $u_r \neq c$. This indicates that, unlike body waves, the ray path of surface waves cannot be described solely by the group velocity and requires consideration of both phase and group velocity directions. A more complex case arises when $\hat{k} \cdot \hat{u} < 0$, which is associated with a decrease in the Maslov index (Tromp and Dahlen, 1993). In such situations, Dijkstra's algorithm becomes unsuitable for ray tracing, as it assumes non-negative edge weights and cannot handle the occurrence of negative travel times in the ray-tracing graph. Instead, the Bellman–Ford algorithm (Bellman, 1958) should be employed, as it is capable of handling graphs with negative weights and can still correctly compute the minimum travel-time paths.

ACKNOWLEDGMENTS

add something here

APPENDIX A

VTI MATRICES AND IMPLEMENTATION DETAILS

In Love wave:

$$M_{ij} = \frac{h_k w_i \rho_i}{2} \delta_{ij}$$

$$K_{ij} = \frac{h_k w_i N_i}{2} \delta_{ij}$$

$$E_{iq} = \left[\sum_{s=1}^n w_s L_s l_i'(\xi^s) l_q'(\xi^s) \right] \frac{2}{h_k}$$
(A-1)

here w_i is the weights for numerical integral, $J_k=\mathrm{d}z/\mathrm{d}\xi$ in k-th element, h_k is the length of k-th element.

For Rayleigh/Scholte Wave:

$$M_{ij} = w_{i}\rho_{i}J_{k}\delta_{ij}; \quad K_{ij}^{1} = w_{i}A_{i}J_{k}\delta_{ij}$$

$$K_{ij}^{2} = w_{j}F_{j}l'_{i}(\xi_{j}) - w_{i}L_{i}l'_{j}(\xi_{i})$$

$$K_{ij}^{3} = w_{i}L_{i}J_{k}\delta_{ij}$$

$$E_{ij}^{1} = J_{k}^{-1}\sum_{m} \left[w_{m}L_{m}l'_{i}(\xi_{m})l'_{j}(\xi_{m})\right]$$

$$E_{ij}^{2} = w_{i}F_{i}l'_{j}(\xi_{i}) - w_{j}L_{j}l'_{i}(\xi_{j})$$

$$E_{ij}^{3} = J_{k}^{-1}\sum_{m} \left[w_{m}C_{m}l'_{j}(\xi_{m})l'_{i}(\xi_{m})\right]$$
(A-2)

APPENDIX B

QUADRATIC EIGENVALUE PROBLEM

Suppose we want to solve the eigenvalue λ of this quadratic eigenvalue problem (QEP):

$$(\lambda^2 \mathbf{K} + \lambda \mathbf{H} + \mathbf{M})\mathbf{x} = \mathbf{0}$$
 (B-1)

We can linearize this system by define two auxiliary matrices and a auxiliary vector \boldsymbol{z} (also called the first companion):

$$\mathbf{A} = \begin{bmatrix} \mathbf{0} & \mathbf{I} \\ -\mathbf{M} & -\mathbf{H} \end{bmatrix} \quad \mathbf{B} = \begin{bmatrix} \mathbf{I} & \mathbf{0} \\ \mathbf{0} & \mathbf{K} \end{bmatrix} \quad \mathbf{z} = \begin{bmatrix} \mathbf{x} \\ \lambda \mathbf{x} \end{bmatrix}$$
(B-2)

It can be verified that the original quadratic eigenvalue problem is equivalent to generalized eigenvalue problem of this new system:

$$\mathbf{A}\mathbf{z} = \lambda \mathbf{B}\mathbf{z} \tag{B-3}$$

For the left eigenvector y, we seek to find the trial solution

$$\boldsymbol{w}^{\dagger} \begin{bmatrix} \mathbf{0} & \boldsymbol{I} \\ -\boldsymbol{M} & -\boldsymbol{H} \end{bmatrix} = \lambda \boldsymbol{w}^{\dagger} \begin{bmatrix} \boldsymbol{I} & \mathbf{0} \\ \mathbf{0} & \boldsymbol{K} \end{bmatrix} \quad \boldsymbol{w}^{\dagger} = \begin{bmatrix} \boldsymbol{y}^{\dagger} \boldsymbol{F} & \boldsymbol{y}^{\dagger} \boldsymbol{G} \end{bmatrix}$$
(B-4)

The matrix F and G are needed to be decided by matching the equation (B-4) with the original QEP problem, then we have:

$$-\mathbf{y}^{\dagger}\mathbf{G}\mathbf{M} = \lambda\mathbf{y}^{\dagger}\mathbf{F}$$
 (B-5)
 $\mathbf{y}^{\dagger}\mathbf{F} - \mathbf{y}^{\dagger}\mathbf{G}\mathbf{H} = \lambda\mathbf{y}^{\dagger}\mathbf{G}\mathbf{K}$

Insert the first equation into the second one, we have

$$\lambda^2 y^{\dagger} G K + \lambda y^{\dagger} G H + y^{\dagger} G M = 0$$
 (B-6)

which means we can choose:

$$\mathbf{F} = -\lambda^{-1}\mathbf{M}; \quad \mathbf{G} = \mathbf{I} \tag{B-7}$$

Therefore, we can only do one Schur decomposition on matrices \boldsymbol{A} and \boldsymbol{B} to obtain the two auxiliary vector \boldsymbol{z} and \boldsymbol{w} , then the first/last segment of it are the eigenvectors we want.

APPENDIX C

DUAL LAGRANGIAN

For visco-elastic medium, we can introduce an anti-dissipation system in which the modulus is the complex conjugate of M_{ijkl} in equation (21). So in time domain, we have:

$$c^{+}(t) = C^{R} \mathcal{F}^{-1} \left[\frac{1}{i\omega} - \sum_{p=1}^{N} \frac{\tau^{p}}{\omega_{p} - i\omega} \right] = C^{R} \left[H(t) - \sum_{p=1}^{N} \tau_{p} e^{\omega_{p} t} H(-t) \right]$$
 (C-1)

So we can write down the PDE for these two systems as:

$$\rho \ddot{u}_{i} = \sigma_{ij,j} = \left[C_{ijkl}^{R} u_{k,l} + C_{ijkl}^{I}(t) * \dot{u}_{k,l} \right]_{,j}$$

$$\rho \ddot{u}_{i}^{+} = \sigma_{ij,j}^{+} = \left[C_{ijkl}^{R} u_{k,l}^{+} - C_{ijkl}^{I}(-t) * \dot{u}_{k,l}^{+} \right]_{,j}$$

$$n_{j} \sigma_{ij}|_{\partial \Omega} = n_{j} \sigma_{ij}^{+}|_{\partial \Omega} = 0$$

$$u_{i}|_{t=0} = \dot{u}_{i}|_{t=0} = u_{i}^{+}|_{t=0} = \dot{u}_{i}^{+}|_{t=0} = 0$$
(C-2)

To determine the Lagrangian of this dual system, we first compute the elastic potential energy density in this system:

$$\Phi = \frac{1}{2} \left(\sigma_{ij} + \sigma_{ij}^{+} \right) \left(u_{i,j} + u_{i,j}^{+} \right)
= \frac{1}{2} \sigma_{ij} u_{i,j} + \frac{1}{2} \sigma_{ij}^{+} u_{i,j}^{+} + \frac{1}{2} \sigma_{ij} u_{i,j}^{+} + \frac{1}{2} \sigma_{ij}^{+} u_{i,j}
= \Phi_{S} + \Phi_{I}$$
(C-3)

where σ_{ij} and σ_{ij}^+ is the stress tensor produced by each system, and Φ_S , Φ_I are called the "self energy" and "dual energy" of this dual system. Note that:

$$\int dV dt \ \Phi_S = -\frac{1}{2} \int dV dt \ \left[\sigma_{ij,j} u_i + \sigma_{ij,j}^+ u_i^+ \right] = -\frac{1}{2} \int dV dt \ \rho \left[\ddot{u}_i u_i + \ddot{u}_i^+ u_i^+ \right]$$

$$= \frac{1}{2} \int dV dt \ \rho \left[\dot{u}_i \dot{u}_i + \dot{u}_i^+ \dot{u}_i^+ \right]$$
(C-4)

And the kinematic energy density can also be divided as "self kinematic energy" and "dual kinematic energy":

$$T = \frac{1}{2}\rho(\dot{u}_i + \dot{u}_i^+)(\dot{u}_i + \dot{u}_i^+) = \left(\frac{1}{2}\rho\dot{u}_i\dot{u}_i + \frac{1}{2}\rho\dot{u}_i^+\dot{u}_i^+\right) + \rho\dot{u}_i\dot{u}_i^+ = T_S + T_I \qquad (C-5)$$

So we can obtain the action:

$$S = \int dV dt \ (T - \Phi) = \int dV dt \ (T_S - \Phi_S) + \int dV dt \ (T_I - \Phi_I)$$
 (C-6)

obviously the first term above equation is 0, so we can define the integrand of the second term (which is only related to dual energy) as the dual Lagrangian:

$$\mathcal{L} = T_I - \Phi_I = \rho \dot{u}_i \dot{u}_i^+ - C_{ijkl}^R u_{k,l} u_{i,j}^+ - \frac{1}{2} C_{ijkl}^I(t) * \dot{u}_{k,l} u_{i,j}^+ + \frac{1}{2} C_{ijkl}^I(-t) * \dot{u}_{k,l}^+ u_{i,j}$$
 (C-7)

Then we can prove the Virial theorem hold for this dual system, i.e. the action is

0. Note:

$$\int dV dt \rho \dot{u}_{i} \dot{u}_{i}^{+} = -\int dV dt \rho \ddot{u}_{i} u_{i}^{+} = -\int dV dt \rho \ddot{u}_{i}^{+} u_{i}$$

$$= \int dV dt \left[C_{ijkl}^{R} u_{k,l} u_{i,j}^{+} + C_{ijkl}^{I}(t) * \dot{u}_{k,l} u_{i,j}^{+} \right]$$

$$= \int dV dt \left[C_{ijkl}^{R} u_{k,l} u_{i,j}^{+} - C_{ijkl}^{I}(-t) * \dot{u}_{k,l}^{+} u_{i,j} \right]$$
(C-8)

So:

$$2S = 2 \int dV dt \mathcal{L} = \int dV dt \left[\frac{1}{2} C_{ijkl}^{I}(t) * \dot{u}_{k,l} u_{i,j}^{+} + \frac{1}{2} C_{ijkl}^{I}(-t) * \dot{u}_{k,l}^{+} u_{i,j} \right]$$

$$+ \int dV dt \left[-\frac{1}{2} C_{ijkl}^{I}(t) * \dot{u}_{k,l} u_{i,j}^{+} - \frac{1}{2} C_{ijkl}^{I}(-t) * \dot{u}_{k,l}^{+} u_{i,j} \right]$$

$$= 0$$
(C-9)

Then under small change of δu_i , the variation of \mathcal{S} is

$$\delta S = \int dV dt \left[\nabla_{u_i} \mathcal{L} \delta u_i + \nabla_{u_{i,j}} \mathcal{L} \delta u_{i,j} \right]$$

$$= \int dV dt \left[\rho \delta \dot{u}_i \dot{u}_i^+ - \frac{1}{2} \left(C_{ijkl}^R u_{k,l}^+ - C_{ijkl}^I (-t) * \dot{u}_{k,l}^+ \right) \delta u_{i,j} \right] -$$

$$\int dV dt \frac{1}{2} \left[C_{ijkl}^R u_{k,l}^+ \delta u_{i,j} + C_{ijkl}^I (t) * \delta \dot{u}_{k,l} u_{i,j}^+ \right]$$

$$= \delta S_1 + \delta S_2$$
(C-10)

Integration by parts:

$$\delta S_1 = \int dV dt \left[-\rho \ddot{u}_i^+ + \frac{1}{2} \left(C_{ijkl}^R u_{k,l}^+ - C_{ijkl}^I (-t) * \dot{u}_{k,l}^+ \right)_{,j} \right] \delta u_i$$
 (C-11)

To compute δS_2 , note that:

$$\int dt \ f'(t) * g(t)h(t) = \int d\tau \ g(\tau) \int dt \ f'(t-\tau)h(t)$$
 (C-12)

We set $f_R(t) = f(-t)$, then:

$$\int dt \ f'(t) * g(t)h(t) = -\int d\tau \ g(\tau) \int dt \ f'_R(\tau - t)h(t)$$

$$= -\int dt \ f'_R(t) * h(t)g(t) = -\int dt \ f_R(t) * h'(t)g(t)$$
(C-13)

So:

$$\int dt \ C_{ijkl}^{I}(t) * \delta \dot{u}_{k,l} u_{i,j}^{+} = \int dt \ \dot{C}_{ijkl}^{I}(t) * \delta u_{k,l} u_{i,j}^{+} = -\int dt \ C_{ijkl}^{I}(-t) * \dot{u}_{i,j}^{+} \delta u_{k,l} \ \text{(C-14)}$$

Then

$$\delta S_2 = \int dV dt \, \frac{1}{2} \left(C_{ijkl}^R u_{k,l}^+ - C_{ijkl}^I (-t) * \dot{u}_{k,l}^+ \right)_{,j} \delta u_i \tag{C-15}$$

So:

$$\delta S = \delta S_1 + \delta S_2 = \int dV dt \left[-\rho \ddot{u}_i^+ + \left(C_{ijkl}^R u_{k,l}^+ - C_{ijkl}^I (-t) * \dot{u}_{k,l}^+ \right)_{,j} \right] \delta u_i = 0 \quad (C-16)$$

where the last equation is by using the wave equation of the anti-dissipation system. The same derivation can also be applied for δu_i^+ . Therefore, expression (C-7) satisfy all requirements of a Lagrangian of a conserved system, we can apply the Rayleigh's principle on this new Lagrangian to obtain derivatives related to phase velocity.

APPENDIX D

SYMMETRY OF SEM MATRICES

we start from the wave equation in frequency domain:

$$-\rho\omega^2 u_i = (c_{ijkl}u_{k,l})_{,j} \tag{D-1}$$

substitute $u_i = U_i(z)e^{i\omega t - i{\bf k}\cdot{\bf r}}$, we have :

$$\nabla_p u_q = (-ik\hat{k}_p U_q + \hat{z}_p \partial_z U_q) e^{i\omega t - i\mathbf{k}\cdot\mathbf{r}}$$
(D-2)

Therefore:

$$-\rho\omega^2 U_i = -ik\hat{k}_j \left[c_{ijpq} (-ik\hat{k}_q U_p + \hat{z}_q \partial_z U_p) \right] + \hat{z}_j \partial_z \left[c_{ijpq} (-ik\hat{k}_q U_p + \hat{z}_q \partial_z U_p) \right]$$
(D-3)

To simplify the analysis below, we can set $\hat{k} = \hat{x}$ and then by the weak form we have:

$$\int \rho \omega^2 U_i \psi \, dz = k^2 \int c_{i1p1} U_p \psi \, dz + \int c_{i3p3} \partial_z U_p \partial_z \psi \, dz + ik \int \left[c_{i1p3} \partial_z U_p \psi - c_{i3p1} U_p \partial_z \psi \right] \, dz$$
(D-4)

Insert the element matrix as:

$$\int_{\Omega_{k}} PU\phi \ dz \Rightarrow P_{ij}^{1} = w_{i}P_{i}J_{k}\delta_{ij}$$

$$\int_{\Omega_{k}} P\partial_{z}U\phi \ dz \Rightarrow P_{ij}^{2} = w_{i}P_{i}l'_{j}(\xi_{i})$$

$$\int_{\Omega_{k}} PU\partial_{z}\phi \ dz \Rightarrow P_{ij}^{3} = w_{j}P_{j}l'_{i}(\xi_{j})$$

$$\int_{\Omega_{k}} P\partial_{z}U\partial_{z}\phi \ dz \Rightarrow P_{ij}^{4} = J_{k}^{-1} \sum_{m} w_{m}P_{m}l'_{j}(\xi_{m})l'_{i}(\xi_{m})$$
(D-5)

we can obtain the matrix form:

$$\omega^2 M x = k^2 K x + k H x + E x \tag{D-6}$$

The element matrices in one element e for are:

$$K_{ab}^{ip} = \omega_{a} c_{i1p1}^{b} J_{e} \delta_{ab}$$

$$E_{ab}^{ip} = J_{e}^{-1} \sum_{s} c_{i3p3}^{s} \omega_{s} l_{b}'(\xi_{s}) l_{a}'(\xi_{s})$$

$$H_{ab}^{ip} = i \left[c_{i1p3}^{a} \omega_{a} l_{b}'(\xi_{a}) - c_{i3p1}^{b} \omega_{b} l_{a}'(\xi_{b}) \right]$$
(D-7)

In SEM, we should assemble each element matrix to a global matrix through the connectivity matrix:

$$A = C(e, a) \tag{D-8}$$

where e is the e-th element and a is the a-th GLL nodes. Now the eigenvector have 3 components, so it will cover $n \times 3$ points in total, where n is the global unique points for wavefield. If we arange the eigenvector in components by components way, i.e.

put the 1st component for the first n points, and then the second components, we can obtain the contribution of (a, b)-th element to global matrix element (A, B) through:

$$A = C(e, a) + (i - 1) * n; \quad B = C(e, b) + (p - 1) * n$$
 (D-9)

So we can get the transpose of global matrix as:

$$K_{BA}^{g} \Rightarrow K_{ba}^{pi} = J^{e}\omega_{b}c_{p1i1}^{a}\delta_{ba} = J^{e}\omega_{a}c_{i1p1}^{b}\delta_{ab} = K_{ab}^{ip} = K_{AB}^{g}$$

$$E_{BA}^{g} \Rightarrow E_{ba}^{pi} = J_{e}^{-1}\sum_{s}c_{i3p3}^{s}\omega_{s}l_{a}'(\xi_{s})l_{b}'(\xi_{s}) = E_{ab}^{ip} = E_{BA}^{g}$$

$$H_{BA}^{g} \Rightarrow H_{ba}^{pi} = i\left[c_{p1i3}^{b}\omega_{b}l_{a}'(\xi_{b}) - c_{p3i1}^{a}\omega_{a}l_{b}'(\xi_{a})\right] = -H_{ab}^{ip} = -H_{AB}^{g}$$
(D-10)

If all elastic parameters are real number, we can know all matrices are Hermitian, this is the in agreement with the facts the linear wave equation operator is self-adjoint.

REFERENCES

- Aki, K., and P. Richards, 2002, Quantitative seismology: University Science Books.
- Al-Attar, D., and O. Crawford, 2016, Particle relabelling transformations in elasto-dynamics: Geophysical Supplements to the Monthly Notices of the Royal Astronomical Society, **205**, 575–593.
- Bellman, R., 1958, On a routing problem: Quarterly of applied mathematics, 16, 87–90.
- Ben-Menahem, A., and S. J. Singh, 2012, Seismic waves and sources: Springer Science & Business Media.
- Blanch, J. O., J. O. Robertsson, and W. W. Symes, 1995, Modeling of a constant q: Methodology and algorithm for an efficient and optimally inexpensive viscoelastic technique: Geophysics, **60**, 176–184.
- Bottero, A., P. Cristini, D. Komatitsch, and M. Asch, 2016, An axisymmetric time-domain spectral-element method for full-wave simulations: Application to ocean acoustics: The journal of the acoustical society of America, **140**, 3520–3530.
- Carcione, J., 1990, Wave propagation in anisotropic linear viscoelastic media: theory and simulated wavefields: Geophysical Journal International, **101**, 739–750.
- ———, 1992, Anisotropic Q and velocity dispersion of finely layered media: Geophys. Prosp., **40**, 40.
- Carcione, J., and F. Cavallini, 1995, Attenuation and quality factor surfaces in anisotropic-viscoelastic media: Mechanics of Materials, 19, 311–327.
- Carcione, J. M., 1995, Constitutive model and wave equations for linear, viscoelastic,

- anisotropic media: Geophysics, 60, 537–548.
- Cerveny, V., 2001, Seismic ray theory: Cambridge University Press.
- Červený, V., and I. Pšenčík, 2008, Quality factor q in dissipative anisotropic media: Geophysics, **73**, T63–T75.
- Chaljub, E., D. Komatitsch, J.-P. Vilotte, Y. Capdeville, B. Valette, and G. Festa, 2007, Spectral-element analysis in seismology: Advances in geophysics, **48**, 365–419.
- Chen, X., 1993, A systematic and efficient method of computing normal modes for multilayered half-space: Geophysical Journal International, 115, 391–409.
- Chevrot, S., 2006, Finite-frequency vectorial tomography: a new method for high-resolution imaging of upper mantle anisotropy: Geophysical Journal International, 165, 641–657.
- Dahlen, F. A., and J. Tromp, 1998, Theoretical Global Seismology: Princeton University Press. NJ.
- Dunkin, J. W., 1965, Computation of modal solutions in layered, elastic media at high frequencies: Bulletin of the Seismological Society of America, **55**, 335–358.
- Gharti, H. N., J. Tromp, and S. Zampini, 2018, Spectral-infinite-element simulations of gravity anomalies: Geophysical Journal International, 215, 1098–1117.
- Giles, M. B., M. C. Duta, J.-D. Muller, and N. A. Pierce, 2003, Algorithm developments for discrete adjoint methods: AIAA journal, 41, 198–205.
- Haney, M. M., and V. C. Tsai, 2017, Perturbational and nonperturbational inversion of rayleigh-wave velocities: Geophysics, 82, F15–F28.
- Hao, Q., and S. Greenhalgh, 2021, Nearly constant q models of the generalized stan-

- dard linear solid type and the corresponding wave equations: Geophysics, 86, T239–T260.
- Haskell, N. A., 1990, The dispersion of surface waves on multilayered media: Vincit veritas: A portrait of the life and work of Norman Abraham Haskell, 1905–1970, 30, 86–103.
- Hawkins, R., 2018, A spectral element method for surface wave dispersion and adjoints: Geophysical Journal International, **215**, 267–302.
- He, X., L.-F. Zhao, X.-B. Xie, X. Tian, and Z.-X. Yao, 2021, Weak crust in southeast tibetan plateau revealed by lg-wave attenuation tomography: Implications for crustal material escape: Journal of Geophysical Research: Solid Earth, 126, e2020JB020748.
- Hesthaven, J. S., 1998, From electrostatics to almost optimal nodal sets for polynomial interpolation in a simplex: SIAM Journal on Numerical Analysis, **35**, 655–676.
- Hu, S., and L. Zhu, 2018, Calculation of differential seismograms using analytic partial derivatives—ii regional waveforms: Geophysical Journal International, 212, 390— 399.
- Keith, C. M., and S. Crampin, 1977, Seismic body waves in anisotropic media: synthetic seismograms: Geophysical Journal International, 49, 225–243.
- Knopoff, L., and M. J. Randall, 1970, The compensated linear-vector dipole: A possible meachnism for deep earthquakes: J. Geophys. Res., **54**, 4957–4963.
- Komatitsch, D., and J. Tromp, 1999, Introduction to the spectral element method for three-dimensional seismic wave propagation: Geophysical journal international, 139, 806–822.

- Kugler, S., T. Bohlen, T. Forbriger, S. Bussat, and G. Klein, 2007, Scholte-wave to-mography for shallow-water marine sediments: Geophysical Journal International, 168, 551–570.
- Lanza, F., C. H. Thurber, E. M. Syracuse, J. A. Power, and A. Ghosh, 2020, Seismic tomography of compressional wave velocity and attenuation structure for makushin volcano, alaska: Journal of Volcanology and Geothermal Research, 393, 106804.
- Li, J., R. L. Weaver, J. Y. Yoritomo, and X. Song, 2020, Application of temporal reweighting to ambient noise cross-correlation for improved seismic green's function: Geophysical Journal International, 221, 265–272.
- Lin, F.-C., M. H. Ritzwoller, and R. Snieder, 2009, Eikonal tomography: surface wave tomography by phase front tracking across a regional broad-band seismic array: Geophysical Journal International, 177, 1091–1110.
- Liu, Q., and J. Tromp, 2006, Finite-frequency kernels based on adjoint methods.: Bull. Seismol. Soc. Am., 96, 2383–2397.
- ——, 2008, Finite-frequency sensitivity kernels for global seismic wave propagation based upon adjoint methods.: Geophys. J. Int., **174**, 265–286.
- Luco, J. E., and R. J. Apsel, 1983, On the green's functions for a layered half-space.

 part i: Bulletin of the Seismological Society of America, 73, 909–929.
- Lyu, C., Y. Capdeville, and L. Zhao, 2020, Efficiency of the spectral element method with very high polynomial degree to solve the elastic wave equation: Geophysics, 85, T33–T43.
- Martin, B., and C. Thomson, 1997, Modelling surface waves in anisotropic structures ii: Examples: Physics of the Earth and Planetary interiors, **103**, 253–279.

- Mensch, T., and V. Farra, 2002, P-wave tomography in inhomogeneous orthorhombic media: Seismic Waves in Laterally Inhomogeneous Media, 1855–1879.
- Nishida, K., J.-P. Montagner, and H. Kawakatsu, 2009, Global surface wave tomography using seismic hum: Science, **326**, 112–112.
- Orta, A. H., M. Kersemans, and K. Van Den Abeele, 2022, A comparative study for calculating dispersion curves in viscoelastic multi-layered plates: Composite Structures, 294, 115779.
- Park, J., 1996, Surface waves in layered anisotropic structures: Geophysical Journal International, 126, 173–183.
- Prindle, K., and T. Tanimoto, 2006, Teleseismic surface wave study for s-wave velocity structure under an array: Southern california: Geophysical Journal International, 166, 601–621.
- Ritzwoller, M. H., and A. L. Levshin, 1998, Eurasian surface wave tomography: Group velocities: Journal of Geophysical Research: Solid Earth, **103**, 4839–4878.
- Sayers, C. M., 2018, Elastic anisotropy of polycrystalline ice with transversely isotropic and orthotropic symmetry: Geophysical Journal International, **215**, 155–164.
- Schwab, F., and L. Knopoff, 1970, Surface-wave dispersion computations: Bulletin of the Seismological Society of America, **60**, 321–344.
- Shapiro, N. M., M. Campillo, L. Stehly, and M. Ritzwoller, 2005, High resolution surface wave tomography from ambient seismic noise: Science, **307**, 1615–1618.
- Shen, W., M. H. Ritzwoller, D. Kang, Y. Kim, F.-C. Lin, J. Ning, W. Wang, Y. Zheng, and L. Zhou, 2016, A seismic reference model for the crust and uppermost mantle

- beneath china from surface wave dispersion: Geophysical Journal International, **206**, 954–979.
- Shen, Z., Y. Yang, X. Fu, K. H. Adams, E. Biondi, and Z. Zhan, 2024, Fiber-optic seismic sensing of vadose zone soil moisture dynamics: Nature Communications, 15, 6432.
- Sherburn, S., R. S. White, and M. Chadwick, 2006, Three-dimensional tomographic imaging of the taranaki volcanoes, new zealand: Geophysical Journal International, 166, 957–969.
- Shi, C., H. Ren, Z. Li, and X. Chen, 2022, Calculation of normal and leaky modes for horizontal stratified models based on a semi-analytical spectral element method: Geophysical Journal International, 230, 1928–1947.
- Smith, M. M., J. Thomson, M. G. Baker, R. E. Abbott, and J. Davis, 2023, Observations of ocean surface wave attenuation in sea ice using seafloor cables: Geophysical Research Letters, **50**, e2023GL105243.
- Takeuchi, H., and M. Saito, 1972, Seismic surface waves: in: Methods in Computational Physics, editor B. A. Bolt, 11, 217–295.
- Thomson, W. T., 1950, Transmission of elastic waves through a stratified solid medium: J. Appl. Phys., **21**, 89–93.
- Tisseur, F., and K. Meerbergen, 2001, The quadratic eigenvalue problem: SIAM review, 43, 235–286.
- Tromp, J., 1994, Surface-wave propagation on a rotating, anisotropic earth: Geophysical Journal International, 117, 141–152.
- Tromp, J., and F. Dahlen, 1993, Maslov theory for surface wave propagation on a

- laterally heterogeneous earth: Geophysical Journal International, 115, 512–528.
- Tromp, J., C. Tape, and Q. Liu, 2005, Seismic tomography, adjoint methods, time reversal and banana-doughnut kernels: Geophys. J. Int., **160**, 195–216.
- Tsvankin, I., 1997, Anisotropic parameters and p-wave velocity for orthorhombic media: Geophysics, **62**, 1292–1309.
- van Driel, M., and T. Nissen-Meyer, 2014, Optimized viscoelastic wave propagation for weakly dissipative media: Geophysical Journal International, **199**, 1078–1093.
- Wang, K., Y. Yang, P. Basini, P. Tong, C. Tape, and Q. Liu, 2018, Refined crustal and uppermost mantle structure of southern california by ambient noise adjoint tomography: Geophysical Journal International, 215, 844–863.
- Wang, Y., Z. Li, Q. You, T. Hao, J. Xing, L. Liu, C. Zhao, X. Li, L. Hu, and P. Somerville, 2016, Shear-wave velocity structure of the shallow sediments in the bohai sea from an ocean-bottom-seismometer survey: Geophysics, 81, ID25–ID36.
- Woodhouse, J., 1974, Surface waves in a laterally varying layered structure: Geophysical Journal International, 37, 461–490.
- Woodhouse, J., and Y. Wong, 1986, Amplitude, phase and path anomalies of mantle waves: Geophysical Journal International, 87, 753–773.
- Woodhouse, J. H., and A. M. Dziewonski, 1984, Mapping the upper mantle: Three-dimensional modeling of earth structure by inversion of seismic waveforms: Journal of Geophysical Research: Solid Earth, 89, 5953–5986.
- Xia, J., R. D. Miller, and C. B. Park, 1999, Estimation of near-surface shear-wave velocity by inversion of rayleigh waves: Geophysics, **64**, 691–700.
- Yang, H., H.-F. Duan, J. Zhu, and Q. Zhao, 2024a, Water effects on elastic s-wave

- propagation and attenuation across single clay-rich rock fractures: insights from ultrasonic measurements: Rock Mechanics and Rock Engineering, 57, 2645–2659.
- Yang, H., Q. Zhao, D. Han, Q. Lei, H. Wu, X. Huang, Z. Chen, and Y. Huang, 2025, Elastic wave propagation and attenuation across cemented rock fractures under tension: International Journal of Rock Mechanics and Mining Sciences, 186, 106024.
- Yang, T., T. Xu, Y. Ai, J. Yang, and H. Yuan, 2024b, Fine crust-mantle structure of the major tectonic boundaries between the north china craton and central asian orogenic belt revealed from rayleigh wave phase velocities and receiver functions:

 Journal of Geophysical Research: Solid Earth, 129, e2024JB028857.
- Zhou, B., and S. Greenhalgh, 2005, 'shortest path'ray tracing for most general 2d/3d anisotropic media: Journal of Geophysics and Engineering, 2, 54–63.
- Zhu, Y., and I. Tsvankin, 2006, Plane-wave propagation in attenuative transversely isotropic media: Geophysics, **71**, T17–T30.